iScience

CellPress
OPEN ACCESS

Article

Peroxisome proliferator activated receptor-γ in osteoblasts controls bone formation and fat mass by regulating sclerostin expression

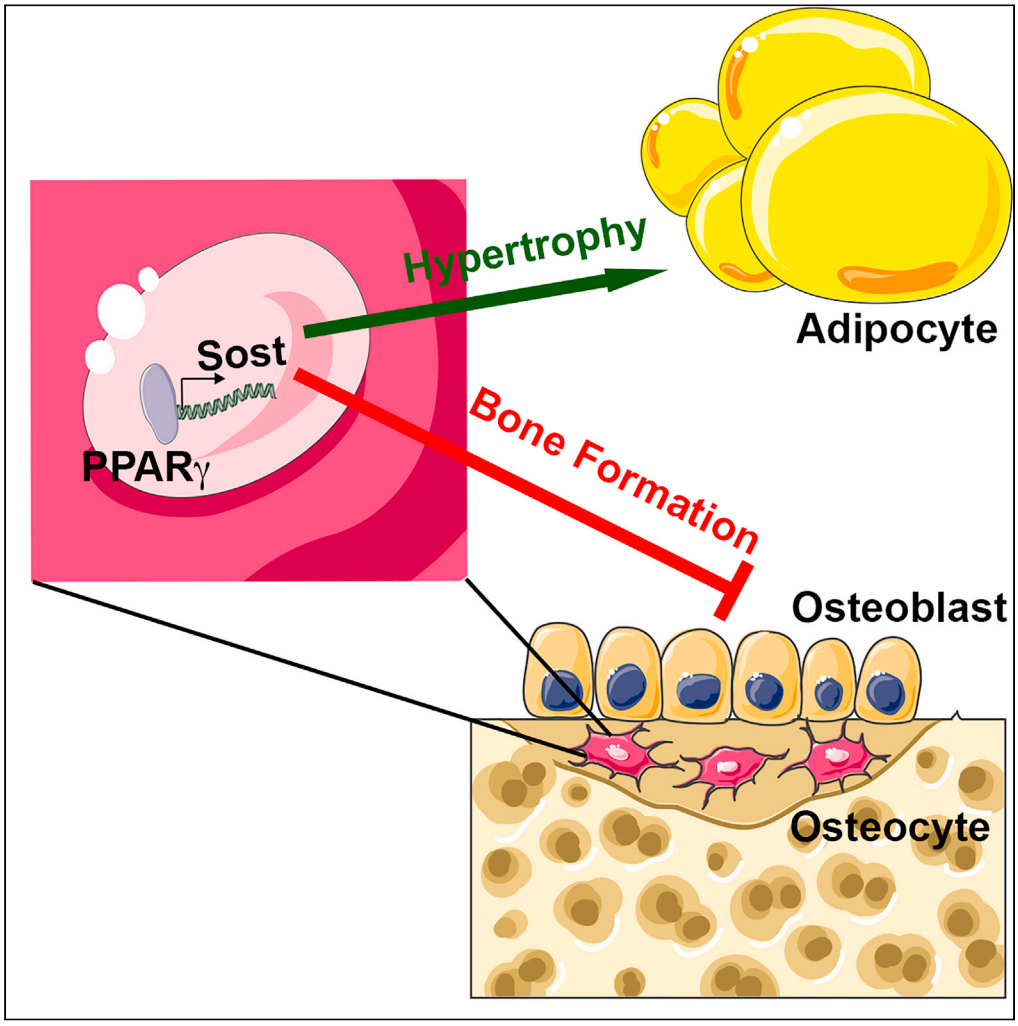

Soohyun P. Kim, Avery H. Seward, Jean Garcia-Diaz, ..., Joseph P. Stains, Michael J. Wolfgang, Ryan C. Riddle

rriddle@som.umaryland.edu

Highlights

PPARγ in osteoblasts and osteocytes regulates bone and fat mass

Mice lacking PPARγ in bone have reduced sclerostin production

Sclerostin contributes to the bone and adipose phenotypes of PPARγ mutant mice

Sclerostin loss of function synergizes with PPARγ to improve metabolism

Kim et al., iScience 26, 106999
July 21, 2023
https://doi.org/10.1016/j.isci.2023.106999

iScience

CellPress
OPEN ACCESS

Article

Peroxisome proliferator activated receptor-γ in osteoblasts controls bone formation and fat mass by regulating sclerostin expression

Soohyun P. Kim,[1] Avery H. Seward,[1] Jean Garcia-Diaz,[1] Nathalie Alekos,[1] Nicole R. Gould,[2] Susan Aja,[3] Joseph P. Stains,[2] Michael J. Wolfgang,[4] and Ryan C. Riddle[1,2,5,6,*]

SUMMARY

The nuclear receptor peroxisome proliferator activated receptor-γ (PPARγ) is a key contributor to metabolic function via its adipogenic and insulin-sensitizing functions, but it has negative effects on skeletal homeostasis. Here, we questioned whether the skeletal and metabolic actions of PPARγ are linked. Ablating *Pparg* expression in osteoblasts and osteocytes produced a high bone mass phenotype, secondary to increased osteoblast activity, and a reduction in subcutaneous fat mass because of reduced fatty acid synthesis and increased fat oxidation. The skeletal and metabolic phenotypes in *Pparg* mutants proceed from the regulation of sclerostin production by PPARγ. Mutants exhibited reductions in skeletal *Sost* expression and serum sclerostin levels while increasing production normalized both phenotypes. Importantly, disrupting the production of sclerostin synergized with the insulin-sensitizing actions of a PPARγ agonist while preventing bone loss. These data suggest that modulating sclerostin action may prevent bone loss associated with anti-diabetic therapies and augment their metabolic actions.

INTRODUCTION

The cycle of osteoclastic resorption and osteoblastic formation that maintains bone mass and strength is strongly influenced by metabolic status. In extreme cases like anorexia nervosa, malnutrition can result in growth arrest and a failure to achieve expected peak bone mass.[1] Similarly, in the less severe but more prevalent conditions of type I and type II diabetes mellitus deviations in glucose homeostasis lead to low bone mineral density or reduced bone quality, respectively, that increase the risk of facture.[2] Understanding the physiologic basis for these interactions will aid in the treatment of the comorbid conditions of obesity, metabolic disease, and osteopenia/osteoporosis.

A primary point of connection between metabolic function and the regulation of bone mass is the direct and indirect action of hormones produced by adipose,[3] muscle,[4] intestine[5] and other tissues on the activity of osteoblasts and osteoclasts. As an example, insulin directly promotes osteoblast differentiation and mice lacking the insulin receptor in osteoblasts exhibit reduced bone volume secondary to deficient numbers of osteoblasts.[6] In turn, osteoblasts and osteocytes secrete factors that influence the metabolic functions of these same tissues.[7] The first evidence for this link was identified in the metabolic actions of osteocalcin. Produced exclusively by mature osteoblasts, osteocalcin regulates insulin production in the pancreas[8,9] as well as the metabolism and performance of skeletal muscle.[10,11]

Sclerostin, a cysteine-knot glycoprotein encoded by the *SOST* gene and produced primarily if not exclusively by matrix-embedded osteocytes, is a major regulator of bone formation as evidenced by the rare bone-overgrowth conditions linked to mutations that prevent its production.[12–14] By binding to the low-density lipoprotein receptor-related protein-5 (LRP5) and LRP6 co-receptors, sclerostin antagonizes the Wnt/β-catenin signaling pathway[15,16] and knockout mice develop a high bone mass phenotype because of enhanced osteoblastic activity.[17] In our previous work, we demonstrated that sclerostin also influences the accumulation of visceral and subcutaneous adipose tissue. $Sost^{-/-}$ mice develop reduced fat mass when fed either a normal diet or a high fat diet and exhibit an increase in insulin sensitivity, whereas sclerostin overproduction stimulates white adipose tissue hypertrophy.[18] These phenotypes are driven by

[1]Department of Orthopaedic Surgery, Johns Hopkins University School of Medicine, Baltimore, MD 21205, USA

[2]Department of Orthopaedics, University of Maryland School of Medicine, Baltimore, MD 21201, USA

[3]Center for Metabolism and Obesity Research, Johns Hopkins University School of Medicine, Baltimore, MD 21205, USA

[4]Department of Biological Chemistry, Johns Hopkins University School of Medicine, Baltimore, MD 21205, USA

[5]Research and Development Service, Baltimore Veterans Administration Medical Center, Baltimore, MD 21201, USA

[6]Lead contact

*Correspondence: rriddle@som.umaryland.edu

https://doi.org/10.1016/j.isci.2023.106999

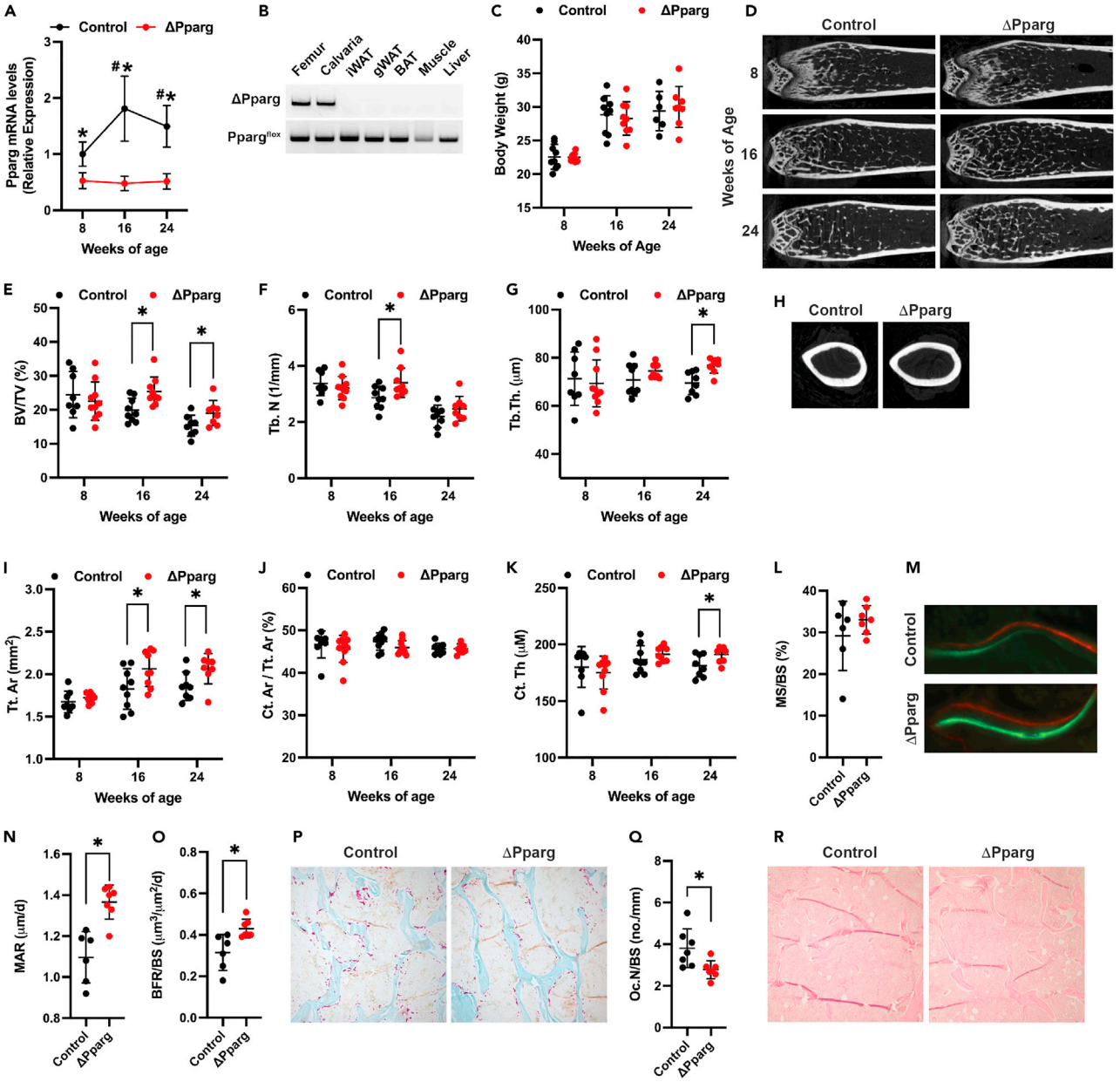

Figure 1. ΔPparg mice develop an increase in bone volume

(A) qPCR analysis of Pparg mRNA levels in the femur of male control and ΔPparg mice (n = 6–8 mice per genotype).

(B) Allele-specific PCR analysis of Pparg gene recombination in tissues isolated from a ΔPparg mouse.

(C) Body weight of male control and ΔPparg mice (n = 6–11 mice per genotype).

(D) Representative microCT images of the distal femur in male control and ΔPparg mice at the indicated ages.

(E–G) MicroCT quantification of trabecular bone volume per tissue volume (BV/TV, E), trabecular number (Tb.N, F) and trabecular thickness (Tb.Th, G) in the distal femur of male control and ΔPparg mice (n = 8–10 mice per genotype).

(H) Representative microCT images of the femoral mid-diaphysis from male 24-week-old control and ΔPparg mice.

(I–K) MicroCT quantification of cortical tissue area (Tt.Ar, I), cortical bone area per tissue area (Ct.Ar/Tt.Ar, J) and cortical thickness (Ct.Th, K) at the femoral mid-diaphysis of control and ΔPparg mice (8–10 mice per genotype).

(L–O) Dynamic histomorphometric quantification of osteoblastic activity in 16-week-old male control and ΔPparg mice including assessment of mineralizing surface per bone surface (MS/BS, L), representative calcein and alizarin red labeled sections (M), mineral apposition rate (MAR, N), and bone formation rate per bone surface (BFR/BS, O) (n = 6–7 mice per genotype).

Figure 1. *Continued*
(P) Representative histological images stained for tartrare-resistant acid phosphate activity (10× original magnification).
(Q) Quantification of osteoclast number per bone surfaces (Oc.N/BS) in the distal femur (7 mice per genotype).
(R) Representative hematoxylin and eosin-stained histological sections to identify marrow adipocytes (10× original magnification). Data presented as mean and standard deviation. *, $p < 0.05$ comparison between control and knockout, #, $p < 0.05$ comparison between an 8-week timepoint and the labeled timepoint in control mice. Data were analyzed by unpaired Student's *t* test.

sclerostin's influence over both the commitment of adipoprogenitors[19] and alterations in the balance of fatty acid synthesis and degradation.[18] Along these lines, serum sclerostin levels in humans have been positively correlated with body mass index in both diabetics and health individuals[20,21] and negatively correlated with parameters of glucose homeostasis.[22–24] These data with the emergence of sclerostin neutralizing antibodies for the treatment of osteopenia/osteoporosis[25,26] raises the possibility that this therapeutic approach could also have positive impacts on both bone and metabolic health. Indeed, sclerostin neutralization in mouse models reduced bone marrow adipogenesis[27] and improves metabolic parameters in mice fed a high fat diet.[18]

Expression of the *Sost* gene in bone is induced by several metabolic insults, including high fat diet feeding,[18,28] inflammation,[28] and hyperglycemia,[29] but little is known about the links between metabolism and sclerostin production. In these studies, we focused on the role of the nuclear receptor peroxisome proliferator activated receptor-γ (PPARγ). In response to a diverse set of endogenous and synthetic ligands PPARγ forms a heterodimer with Retinoid X Receptor α and then acts to regulate the expression of genes involved in both cellular and whole-body metabolism.[30–32] Early studies indicated that PPARγ is sufficient to induce adipogenic differentiation *in vitro*,[33] whereas ablating the expression of *Pparg* in AdipoQ^{+} cells resulted in lipoatrophy, hyperglycemia and severe insulin resistance.[34] *Pparg* is also expressed in cells of the osteoblast lineage and the activation of the nuclear receptor in these cells is widely considered to be detrimental to overall skeletal health. PPARγ favors the adipogenic differentiation of marrow progenitor cells over that of osteoblastic differentiation[35,36] and synthetic agonists increase fracture risk.[37] In addition, several genetic mouse models in which PPARγ function has been abolished or decreased develop a high bone mass phenotype that may be related to altered sclerostin expression because PPAR response elements are present in the *Sost* gene promoter.[38–40]

Here, we hypothesized that PPARγ in osteoblasts and osteocytes provides a mechanistic link between skeletal mass and metabolic function via the transcription factor's regulation of sclerostin production. We find that genetic ablation of the *Pparg* gene in mature bone cells results in the development of a high bone mass phenotype and striking reduction in subcutaneous fat mass. These phenotypes coincide with diminished *Sost* gene expression and serum sclerostin levels and are rescued by adeno-associated virus driven sclerostin overproduction. Moreover, diminishing *Sost* gene expression in bone provides protection against bone loss induced by therapeutic activation of PPARγ while synergistically improving insulin sensitivity.

RESULTS

PPARγ-deficiency in osteoblasts and osteocytes increase bone formation

To determine if PPARγ coordinately regulates skeletal and metabolic homeostasis, we generated mice in which the *Pparg* gene was selectively ablated in osteoblasts and osteocytes. Control (Pparg$^{loxP/loxP}$) and osteoblast/osteocyte-specific mutants (Ocn-Cre$^{TG/+}$; Pparg$^{loxP/loxP}$, hereafter referred to as ΔPparg) were born at the expected Mendelian frequency and exhibited no gross anatomical phenotypes. Although *Pparg* mRNA levels increased with age in the femurs of male controls, expression levels were consistently reduced in mutants (~50–80%, Figure 1A). *Pparg* gene recombination was detected only in the skeletal tissue of ΔPparg mice (Figure 1B) and body weight was similar in controls and knockouts at all timepoints examined (Figure 1C).

Parameters of bone architecture in the distal femur were similar to controls in young, male ΔPparg mice (8 weeks), but as mice aged microCT analyses revealed the development of a high bone mass phenotype in mutants (Figures 1D–1G). Relative to control littermates, trabecular bone volume per tissue volume was increased by 27.5%, secondary to a significant increase in trabecular number, and by 24.1%, secondary to a significant increase in trabecular thickness, in 16- and 24-week-old ΔPparg mice, respectively. Cortical bone at the femoral mid-diaphysis exhibited similar age-related changes in structure as tissue

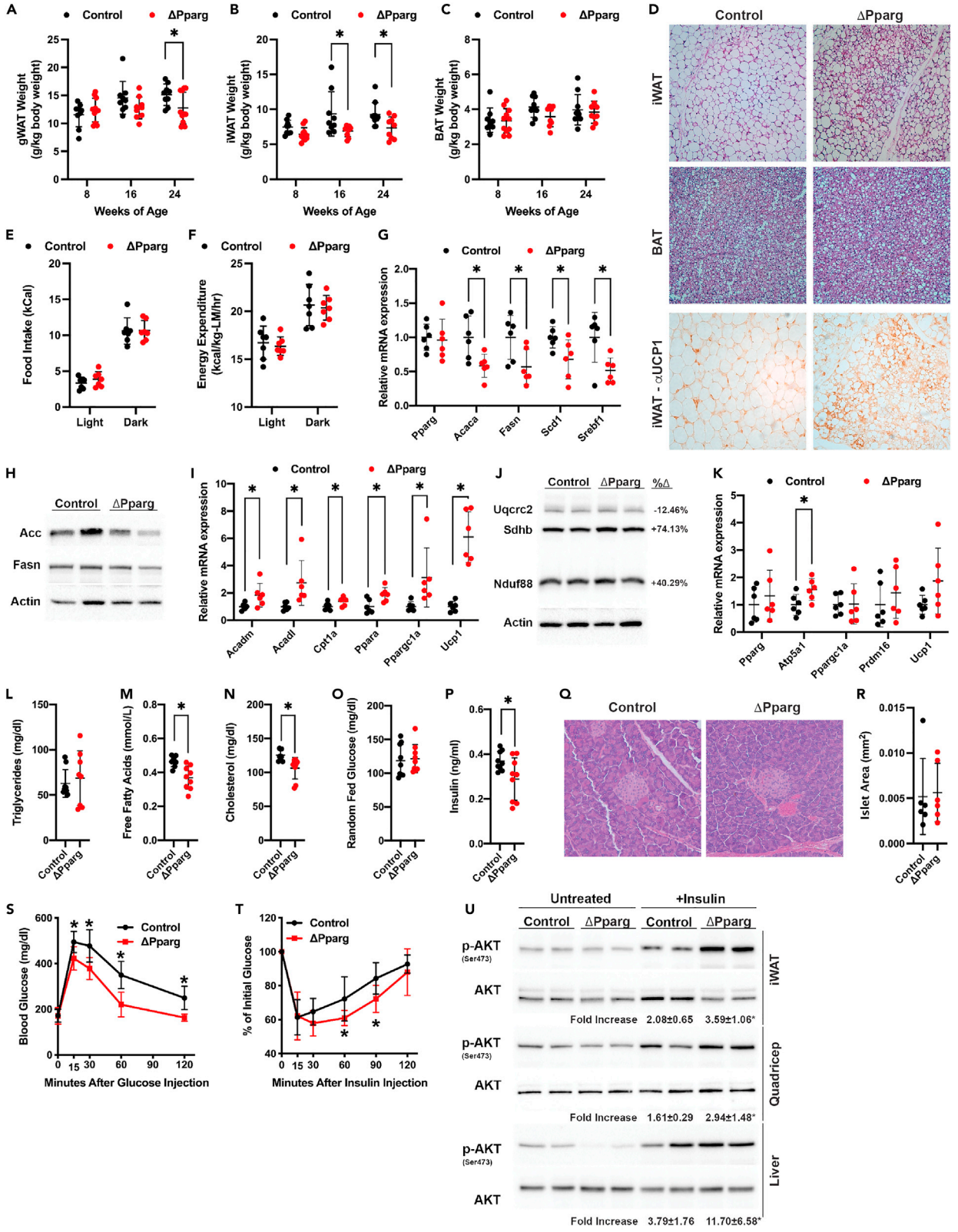
A
Control
ΔPparg
gWAT Weight (g/kg body weight)
Weeks of Age
B
iWAT Weight (g/kg body weight)
C
BAT Weight (g/kg body weight)
D
Control
ΔPparg
iWAT
BAT
iWAT - αUCP1
E
Food Intake (kCal)
Light
Dark
F
Energy Expenditure (kcal/kg-LM/hr)
G
Relative mRNA expression
Pparg
Acaca
Fasn
Scd1
Srebf1
H
Acc
Fasn
Actin
I
Acadm
Acadl
Cpt1a
Ppara
Ppargc1a
Ucp1
J
%Δ
Uqcrc2
-12.46%
Sdhb
+74.13%
Nduf88
+40.29%
K
Atp5a1
Prdm16
L
Triglycerides (mg/dl)
M
Free Fatty Acids (mmol/L)
N
Cholesterol (mg/dl)
O
Random Fed Glucose (mg/dl)
P
Insulin (ng/ml)
Q
R
Islet Area (mm²)
S
Blood Glucose (mg/dl)
Minutes After Glucose Injection
T
% of Initial Glucose
Minutes After Insulin Injection
U
Untreated
+Insulin
p-AKT (Ser473)
AKT
Fold Increase 2.08±0.65 3.59±1.06*
Fold Increase 1.61±0.29 2.94±1.48*
Fold Increase 3.79±1.76 11.70±6.58*
Quadricep
Liver

Figure 2. ΔPparg mice have reduced fat mass and increase insulin sensitivity

(A–C) Mass of the gonadal (gWAT, A), inguinal (iWAT, B), and intrascapular brown (BAT, C) adipose were assessed in male control and ΔPparg mice and normalized to body weight (n = 9–11 mice per genotype).

(D) Representative histological sections of iWAT and BAT stained with hematoxylin and eosin or immunostained for UCP1 expression (10× original magnification) from 16-week-old male mice.

(E) Food intake during 12 h light and dark periods (n = 7 mice per genotype).

(F) Energy expenditure assessed by indirect calorimetry (n = 7 mice per genotype).

(G and I) qPCR analysis of gene expression in iWAT isolated from 16-week-old male mice (n = 6 mice per genotype).

(H and J) Representative western blot analysis of protein expression in iWAT.

(K) qPCR analysis of gene expression in intrascapular brown adipose tissue (n = 6 mice per genotype).

(L–N) Random fed serum lipid analysis in 16-week-old male control and ΔPparg mice (n = 8–9 mice per genotype).

(O and P) Random fed glucose and serum insulin levels (n = 9 mice per genotype).

(Q and R). Representative hematoxylin and eosin stained histological sections of pancreatic b-cell islets (20× original magnification) and quantification of islet area (n = 6 mice per genotype).

(S and T) Glucose tolerance (S) and insulin tolerance (T) test at age 16 weeks(n = 8–9 mice per genotype).

(U) Western blot analysis of AKT phosphorylation in iWAT, quadriceps and liver before and after insulin injection. Fold change in phosphorylation levels relative to untreated samples are show for each tissue (n = 8 mice per genotype). Data presented as mean and standard deviation. *, $p < 0.05$. Data were analyzed by unpaired Student's *t* test.

cross-sectional area was comparable to controls at age 8 weeks, but significantly increased in ΔPparg mice at ages 16 and 24 weeks (Figures 1H–1K). Histomorphometric analyses performed in 16-week male control and ΔPparg mice indicated the increase in trabecular bone volume was because of enhanced osteoblastic activity (Figures 1L–1O), as evidenced by an increase in the mineral apposition rate and bone formation rate, and a decrease in osteoclast numbers (Figures 1P and 1Q). The abundance of marrow adipocytes in the distal femur of control and ΔPparg mice was similar (Figure 1R).

Similar to the loss of PPARγ function in osteoblasts and osteocytes *in vivo*, ablating the expression of *Pparg* in cultures of calvarial osteoblasts increased osteoblast differentiation. Compared to control osteoblasts, ΔPparg osteoblasts exhibited increased staining for alkaline phosphatase activity and matrix mineralization as well as increased expression of *Runx2*, *Atf4*, and *Bglap2* (Figure S1D). Expression of *Tnfsf11* (rank ligand) was not affected by *Pparg* deletion but the levels of *Tnfrsf11b* (osteoprotegerin) were increased (Figure S1E), which may explain the reduced numbers of osteoclasts observed *in vivo*. Therefore, PPARγ in maturing osteoblasts and osteocytes influences skeletal structure by regulating the balance of osteoblastic activity and osteoclast development.

PPARγ-deficiency in osteoblasts and osteocytes reduced fat mass and improves whole body metabolism

Assessment of organ and tissue weights by necropsy indicated that ablating *Pparg* expression in osteoblasts and osteocytes also influenced body composition. When compared to control littermates, gonadal fat pad (gWAT) weight was reduced in 24-week-old male ΔPparg mice (Figure 2A) and inguinal fat pad (iWAT) weight was reduced in both 16- and 24-week-old mutants (Figure 2B). Histological examination of iWAT demonstrated that the reduction in tissue mass in ΔPparg mice was associated with a decrease in adipocyte size and a dramatic increase in the abundance of multilocular cells (Figure 2D). Intrascapular brown adipose tissue (BAT) mass and morphometry (Figures 2C and 2D) and the weights of other major organs (Figures S2A–S2C) in ΔPparg mice were comparable to controls.

The reduction in white adipose tissue mass was not associated with a detectable change in feeding behavior, activity levels, or overall energy expenditure (Figures 2E, 2F, and S2D–S2F). However, gene expression analyses in iWAT suggested that loss of PPARγ function in bone cells altered the ratio of anabolic and catabolic metabolism in white adipose tissue. The expression of genes associated with fatty acid synthesis, including *Acaca* and *Fasn*, were decreased (Figures 2G and 2H) while genes associated with fatty acid oxidation (*Acadl*, *Cpt1a*, and *Ppara*, Figure 2I) were increased in ΔPparg mice when compared to controls. Furthermore, gene markers of brown adipocytes (*Ppargc1a* and *Ucp1*, Figure 2I), UCP1 immunostaining (Figure 2D), and the abundance of mitochondrial proteins (Figure 2J) were increased in iWAT of ΔPparg mice suggesting the induction of beiging in this white adipose tissue depot. Except for a modest, but significant increase in the expression of *Atp5a1*, the expression of brown adipose gene markers in BAT was not affected by *Pparg* gene deletion in osteoblasts and osteocytes (Figure 2K), which is consistent with the normal mass and morphometry of this tissue.

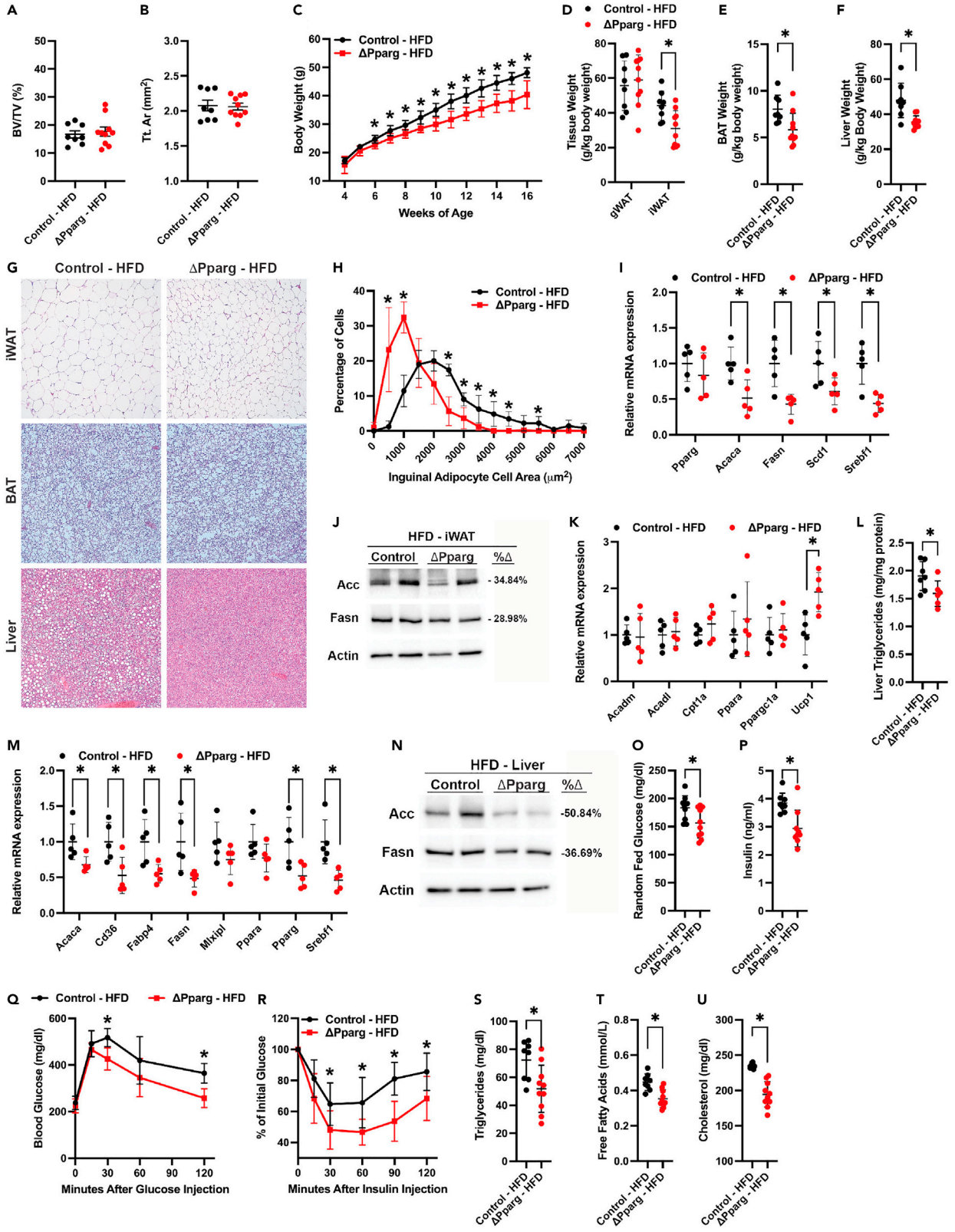
A
BV/TV (%)
Control - HFD
ΔPparg - HFD
B
Tt. Ar (mm²)
C
Body Weight (g)
Weeks of Age
D
Tissue Weight (g/kg body weight)
gWAT
iWAT
E
BAT Weight (g/kg body weight)
F
Liver Weight (g/kg Body Weight)
G
iWAT
BAT
Liver
H
Percentage of Cells
Inguinal Adipocyte Cell Area (μm²)
I
Relative mRNA expression
Pparg
Acaca
Fasn
Scd1
Srebf1
J
HFD - iWAT
Control
ΔPparg
%Δ
Acc
Fasn
Actin
- 34.84%
- 28.98%
K
Acadm
Acadl
Cpt1a
Ppara
Ppargc1a
Ucp1
L
Liver Triglycerides (mg/mg protein)
M
Acaca
Cd36
Fabp4
Fasn
Mlxipl
Ppara
Pparg
Srebf1
N
HFD - Liver
-50.84%
-36.69%
O
Random Fed Glucose (mg/dl)
P
Insulin (ng/ml)
Q
Blood Glucose (mg/dl)
Minutes After Glucose Injection
R
% of Initial Glucose
Minutes After Insulin Injection
S
Triglycerides (mg/dl)
T
Free Fatty Acids (mmol/L)
U
Cholesterol (mg/dl)

Figure 3. ΔPparg mice are resistant to high fat diet feeding

Male control and ΔPparg mice were fed a high fat diet (60% kcal from fat) from ages 4 to 16 weeks.

(A and B) MicroCT quantification of trabecular bone volume per tissue volume (BV/TV) in the distal femur (A) and cortical tissue area (Tt.Ar, B, (n = 8 mice per genotype)).

(C) Weekly assessment of body weights in control and ΔPparg mice fed a high fat diet (n = 9–10 mice per genotype).

(D–F) Mass of white adipose tissue depots (D), BAT (E), and liver (F) normalized to body weight (n = 8–10 mice per genotype).

(G) Representative hematoxylin and eosin histological sections of iWAT, BAT, and liver (10× original magnification).

(H) Size distribution of adipocytes in histological sections of iWAT (n = 5 mice per genotype).

(I–K) qPCR and western blot analysis of genes (I) and proteins (J) involved in fatty acid synthesis and genes involved in fatty acid catabolism or beiging (K) (n = 6 mice per genotype).

(L) Quantification of triglycerides liver tissue (n = 8–10 mice per genotype).

(M and N) qPCR and western blot analysis of genes and proteins involved in fatty acid synthesis and steatosis in the liver of high fat diet fed control and ΔPparg mice (n = 6 mice per genotype).

(O and P) Random fed glucose and insulin levels (n = 8–10 mice per genotype).

(Q and R) Glucose tolerance (Q) and insulin tolerance test (R) after 12 weeks of high-fat diet feeding (n = 8–10 mice per genotype).

(S–U) Random fed serum lipid analysis in high fat diet fed control and ΔPparg mice (n = 8–10 mice per genotype). Data presented as mean and standard deviation. *, $p < 0.05$. Data were analyzed by unpaired Student's *t* test.

Analysis of serum metabolites indicated that ΔPparg mice also developed improvements in lipid and glucose metabolism. Serum triglycerides (Figure 2L) were comparable in control and ΔPparg mice, but free fatty acid and cholesterol levels were reduced (Figures 2M and 2N). Random fed glucose levels and pancreatic β-cell islet morphology were normal in the mutants, but serum insulin was significantly lower which suggests that ΔPparg mice have an increase in insulin sensitivity (Figures 2O–2R). Indeed, glucose excursions during glucose tolerance testing were dampened in ΔPparg mice relative to controls (Figure 2S) and glucose levels were reduced to a greater degree during insulin tolerance testing (Figure 2T). Moreover, the ability of insulin to stimulate AKT phosphorylation was enhanced in iWAT, the quadriceps, and liver of ΔPparg mice relative to control littermates (Figure 2U).

Female ΔPparg mice exhibited similar skeletal and metabolic phenotypes (Figure S3). When examined at age 16 weeks, cortical bone cross-sectional area was significantly increased and the mass of white adipose tissue depots were reduced in female mutants when compared to controls. Likewise, serum insulin levels were lower in female ΔPparg mice which displayed an increased sensitivity to insulin during an insulin tolerance test. Thus, PPARγ in osteoblasts and osteocytes simultaneously influences body composition, whole body metabolism and bone mass.

ΔPparg mice are resistant to the effects of high fat diet on metabolism

To further examine the effect of *Pparg* gene deletion in osteoblasts and osteocytes on metabolism, we next challenged male mutants and control littermates with a high fat diet (HFD, 60% kcal from fat) from ages 4 to 16 weeks. Surprisingly, HFD feeding abolished the effect of PPARγ-deficiency on bone structure as both trabecular bone volume in the distal femur (Figure 3A) and cortical tissue area at the femoral mid-diaphysis were comparable to controls (Figure 3B). Because trabecular bone volume was increased in mutants fed a chow diet (Figure 1E), the normalization of bone volume to controls after HFD feeding represented a more substantial suppression of accrual in mutants (% change in BV/TV from chow fed mice, $-16.21 \pm 18.07\%$ versus $-34.70 \pm 16.36\%$, $p = 0.042$, Mean ± SD). In the cortical bone compartment, the normalization of tissue area between HFD-fed controls and mutants was driven by increases in cortical apposition in control mice (% change in Tt. Ar from chow fed mice, $13.70 \pm 11.89\%$ versus $-0.92 \pm 7.37\%$, $p = 0.007$) likely secondary to the increased body weight associated with HFD feeding.

By contrast, the influence of PPARγ-deficiency on body composition and metabolism were retained after HFD feeding. During the 12-week study, ΔPparg mice exhibited a significant reduction in weight gain (Figure 3C) and had reduced iWAT, BAT, and liver weight (Figures 3D–3F and S4A). As in chow-fed mice, histological and molecular analyses demonstrated that inguinal adipocyte size was reduced in HFD-fed ΔPparg mice relative to controls in association with reduced gene markers of fatty acid synthesis (Figures 3G–3J). The expression of genes involved in fatty acid oxidation and beiging were comparable in HFD-fed ΔPparg mice and controls except for *Ucp1* expression which remained elevated in the iWAT of mutants but with a considerably lower relative change in expression than that in chow-fed mice (Figures 2I and 3K). Adipocyte size in gWAT was similar in HFD-fed control and ΔPparg mice (despite reductions in the expression of genes involved in fatty acid synthesis), but there was a marked reduction in histological and gene expression markers of inflammation (Figures S4B–S4E). In the liver, the accumulation

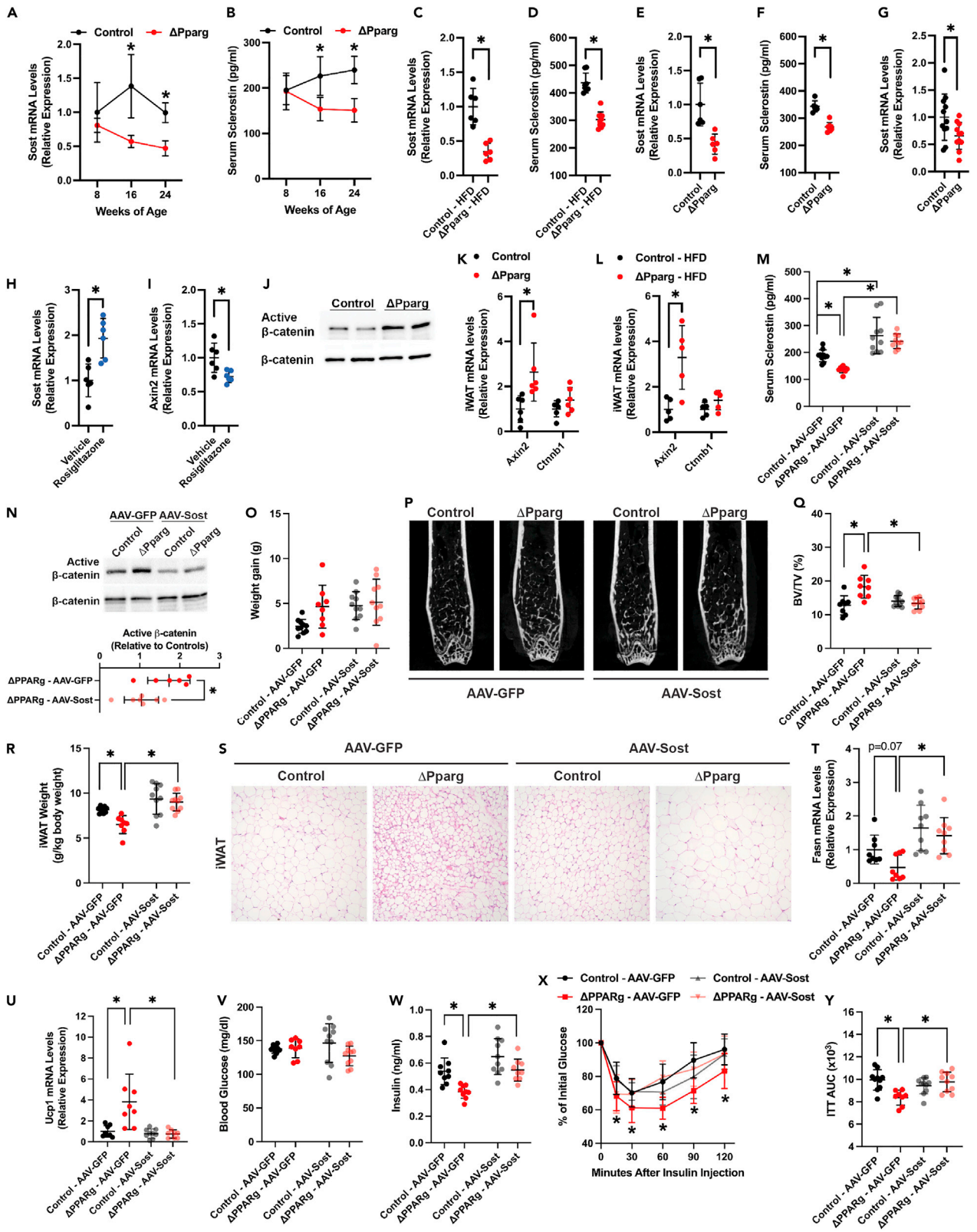
A
Control
ΔPparg
Sost mRNA Levels (Relative Expression)
Weeks of Age
B
Serum Sclerostin (pg/ml)
C
D
E
F
G
H
Vehicle
Rosiglitazone
I
Axin2 mRNA Levels (Relative Expression)
J
Active β-catenin
β-catenin
K
iWAT mRNA levels (Relative Expression)
Axin2
Ctnnb1
L
Control - HFD
ΔPparg - HFD
M
Control - AAV-GFP
ΔPPARg - AAV-GFP
Control - AAV-Sost
ΔPPARg - AAV-Sost
N
AAV-GFP
AAV-Sost
Active β-catenin (Relative to Controls)
O
Weight gain (g)
P
AAV-GFP
AAV-Sost
Q
BV/TV (%)
R
iWAT Weight (g/kg body weight)
S
iWAT
T
p=0.07
Fasn mRNA Levels (Relative Expression)
U
Ucp1 mRNA Levels (Relative Expression)
V
Blood Glucose (mg/dl)
W
Insulin (ng/ml)
X
% of Initial Glucose
Minutes After Insulin Injection
Y
ITT AUC (x10³)

Figure 4. PPARγ in osteoblasts regulated sclerostin production to influence metabolism

(A) qPCR analysis of Sost mRNA levels in the femur of male control and ΔPparg mice (n = 6–8 mice per genotype).
(B) Quantification of serum sclerostin levels in male control and ΔPparg mice (n = 6–8 mice per genotype).
(C and D) Sost mRNA levels (n = 6 mice per genotype, C) and serum sclerostin levels (n = 8–10 mice per genotype, D) were quantified in male control and ΔPparg mice fed a high fat diet (60% kcal from fat) from ages 4 to 16 weeks.
(E and F) Sost mRNA levels (n = 6 mice per genotype, C) and serum sclerostin levels (n = 6–8 mice per genotype, D) were quantified in female control and ΔPparg mice.
(G) qPCR analysis of Sost mRNA levels in cultures of control and ΔPparg primary osteoblasts after 14 days of differentiation (n = 11 samples per group).
(H and I) qPCR analysis of Sost (H) and Axin2 (I) mRNA levels in Ocy454 cells 24 h after treatment with vehicle or rosiglitazone (n = 6 samples per group).
(J) Western blot analysis of active, non-phosphorylated b-catenin and total b-catenin in the iWAT of 16-week-old male control and ΔPparg mice.
(K and L) qPCR analysis of Axin2 and Ctnnb1 mRNA levels in the iWAT of control and ΔPparg mice fed a chow diet (K) or a high fat diet from ages 4 to 16 weeks (n = 5–6 mice per genotype).
(M–Y) 8-week-old control and ΔPparg mice were injected with AAV-8 constructs directing the expression of Sost or GFP and then aged for an additional 8 weeks. (M) Serum sclerostin levels (n = 8–10 mice per group). (N) Western blot analysis of active, non-phosphorylated β-catenin and total β-catenin in the iWAT. (O) Weight gained during the 8-week experiment (n = 8–10 mice per group). (P and Q) Representative microCT images of the distal femur and quantification of trabecular bone volume (n = 8–10 mice per group). (R) iWAT mass (n = 8–10 mice per group). (S) Representative hematoxylin and eosin histological sections of iWAT (10× original magnification). (T and U) qPCR analysis of Fasn and Ucp1 mRNA levels in iWAT (n = 8–9 mice per group). (V) Random fed blood glucose (n = 8–10 mice per group). (W) Serum insulin levels (n = 8–10 mice per group). (X and Y) Insulin tolerance testing and area under the curve analysis (n = 8–10 mice per group). Data presented as mean and standard deviation. *, $p < 0.05$. Data were analyzed by unpaired Student's *t* test or Anova followed by Tukey's multiple comparison post hoc test.

of triglycerides was reduced in HFD-fed ΔPparg mice in association with decreased marker of lipid synthesis and steatosis (Figures 3G and 3L–3N).

The reductions in fat mass and lipid accumulation in ΔPparg mice likely contributed to the maintenance of improved glucose and lipid metabolism that mirrored that in chow-fed mutants. Relative to HFD-fed control littermates, ΔPparg mice exhibit lower random fed glucose and insulin levels (Figures 3O and 3P) and improved performance in both glucose tolerance and insulin tolerance tests (Figures 3Q and 3R). Likewise, serum levels of triglycerides, fatty acids and cholesterol were reduced in HFD-fed ΔPparg mice (Figures 3S–3U). Therefore, ablating the expression of *Pparg* in osteoblasts and osteocytes is sufficient to improve metabolism in the face of an obesogenic stimuli even though it does not protect bone structure from the deleterious effects of this stimuli.

Reductions in sclerostin expression contribute to the metabolic phenotypes of ΔPparg mice

The similarities between the metabolic phenotypes of ΔPparg mice and those we observed previously in $Sost^{-/-}$ mice,[18] including reduced fat mass with altered catabolic and anabolic metabolism in adipocytes, increased insulin sensitivity, and resistance to metabolic disturbances induce by high fat diet feeding, led us to speculate that PPARγ in osteoblasts and osteocytes regulates metabolism through the regulation of sclerostin production. To test this idea, we first examined the effect of ablating *Pparg* expression in osteoblasts and osteocytes on *Sost* mRNA levels in the femur and on serum sclerostin levels. Similar to the delayed effect of PPARγ-deficiency on bone structure, *Sost* mRNA level in 8-week-old male ΔPparg mice were equivalent to those in control littermates but were significantly reduced in the mutants at age 16 weeks ($-58.60 \pm 4.48\%$) and age 24 weeks ($-52.95 \pm 10.05\%$, Figure 4A). Serum sclerostin levels followed a nearly identical pattern (Figure 4B). Similar reductions in *Sost* mRNA level and sclerostin serum abundance were also evident in HFD-fed ΔPparg mice (Figures 4C and 4D) and in female ΔPparg mice (Figures 4E and 4F) when compared to their respective littermate controls. To ensure that regulation of *Sost* was a direct effect of PPARγ function, we examine expression levels in the Ocy454 osteocyte cell model after treatment with the PPARγ-agonist rosiglitazone and in cultures of primary osteoblasts expressing or lacking PPARγ that had been differentiated for 14 days. Rosiglitazone treatment increased *Sost* mRNA levels and decreased the expression of Axin2, indicative of a concomitant suppression of Wnt signaling,[41] in Ocy454 cells (Figures 4H and 4I), whereas ΔPparg osteoblasts exhibited lower *Sost* mRNA levels (Figure 4G). These data and those from Baroi et al.,[38] who document binding of PPARγ to PPRE elements in the *Sost* promoter, indicate a direct regulation of *Sost* expression by PPARγ.

Next, we examined whether Wnt/β-catenin signaling, the primary target of sclerostin, was increased in adipose tissue of ΔPparg mice. In line with the reduced sclerostin serum abundance in ΔPparg mice, the levels of active, non-phosphorylated β-catenin were markedly increased in the iWAT of ΔPparg mice (Figure 4J). Likewise, mRNA levels of *Axin2* were increased in the iWAT of ΔPparg mice fed a chow (Figure 4K) or high fat diet (Figure 4L). By contrast, activation of bone morphogenetic protein (BMP) signaling, a pathway

sclerostin was initially thought to regulate,[42] was reduced in iWAT when indexed by the phosphorylation of SMAD1/5/9 and the mRNA levels of *Bmp4* (Figure S5). The enhancement of Wnt/β-catenin signaling and reduced BMP signaling in the iWAT of ΔPparg mice are consistent with our previous findings in Sost$^{-/-}$ mice.[18]

Finally, to test the primacy of reduced sclerostin availability to the changes in bone structure, body composition and metabolism evident in ΔPparg mice, we attempted to rescue these phenotypes by directing sclerostin overproduction.[18] Cohorts of 8-week-old male control and ΔPparg mice were injected with adeno-associated virus-8 constructs containing a *Sost* cDNA (AAV-Sost) or green fluorescent protein cDNA (AAV-GFP) and then examined at age 16 weeks. Injection of AAV-Sost increased serum sclerostin levels by 39.76 ± 36.15% in control mice and by 77.53 ± 19.96% in ΔPparg mice when compared to those injected with AAV-GFP and thereby normalized serum sclerostin levels between the AAV-Sost groups (Figure 4M) and maintained them at a level lower than those measured in high-fat diet–fed mice (Figure 4D). Importantly, the increased serum sclerostin levels reduced the abundance of active β-catenin in iWAT associated with *Pparg* gene deletion in osteoblasts and osteocytes. (Figure 4N).

Changes in body weight over the 8-week experiment were not statistically different among the 4 groups (Figure 4O), but the increase in serum sclerostin was sufficient to normalize bone structure in ΔPparg mice. Whereas ΔPparg-AAV-GFP mice exhibited an increase in trabecular bone volume secondary to an increase in trabecular number when compared to Control-AAV-GFP mice, all parameters of bone structure were similar in Control-AAV-Sost and ΔPparg-AAV-Sost mice (Figures 4P, 4Q, S6A, and S6B). Similarly, analysis of tissue weights and morphometry after necropsy revealed that iWAT mass and adipocyte morphology in ΔPparg-AAV-Sost were now comparable to that in Control-AAV-Sost (Figures 4R and 4S). This was accompanied by a reversal of the reduced expression of *Fasn* and increased expression of *Ucp1* in ΔPparg-AAV-GFP when compared to Control-AAV-GFP mice (Figures 4T and 4U). The increase in serum sclerostin levels significantly increased gWAT and BAT mass in Control-AAV-Sost versus Control-AAV-GFP mice as we observed previously,[18] but there was not a statistically significant difference between either of the ΔPparg groups (Figures S6C and S6D). The mass of lean tissues was equivalent across all 4 groups (Figure S6E).

Raising serum sclerostin levels via administration of AAV-Sost was also sufficient to normalize glucose and lipid homeostasis. Random fed blood glucose levels were similar across the 4 groups (Figure 4V), but the reduction in serum insulin evident in ΔPparg-AAV-GFP mice was returned to a level comparable to Control-AAV-GFP and Control-AAV-Sost mice (Figure 4W). Similarly, the increase in insulin sensitivity evident in ΔPparg-AAV-GFP mice was corrected by administration of AAV-Sost (Figures 4X and 4Y). Serum lipid levels followed an identical pattern as the reductions in fatty acids and cholesterol in ΔPparg-AAV-GFP mice were returned to normal levels with increased serum sclerostin (Figures S6H and S6I). Taken together, these data highlight an essential role of sclerostin in the influence of PPARγ in osteoblasts and osteocytes on skeletal and metabolic homeostasis.

Sclerostin-deficiency synergizes with PPARγ activation

Because the use of PPARγ agonists like thiazolidinediones that held promise as insulin sensitivers has been limited because of significant cardiovascular and skeletal side effects[37,43] and PPARγ in osteoblasts and osteocytes appears to regulate the skeletal and endocrine actions of sclerostin, we questioned whether suppression of *Sost* gene expression would rescue the skeletal effects and synergize with the metabolic actions of PPARγ activation by rosiglitazone (Rosi). To examine this interaction, 4-week-old male control (Sost$^{iCOIN/iCOIN}$) and ObΔSost (Ocn-Cre$^{TG/+}$; Sost$^{iCOIN/iCOIN}$) mice[19,44,45] were fed a HFD (60% kcal from fat) for 4 weeks to induce obesity and insulin resistance (lead-in) and then randomly assigned to HFD or HFD+Rosi for an additional 8 weeks (Treatment, Figure 5A). As expected, Rosi increased *Sost* mRNA levels and serum sclerostin levels in control mice but had no effect in ObΔSost mice which had substantially lower serum sclerostin levels (Figures 5B and 5C).

Over the 12-week study, control and ObΔSost mice maintained on the HFD or an HFD with Rosi exhibited similar increases in body weight (Figure 5D). iWAT and BAT weights were significantly reduced or trended lower, respectively, in ObΔSost mice relative to control mice maintained on the HFD, but Rosi produced similar relative increases in the mass of each tissue (Figures 5E and 5F). However, striking differences were evident in the morphology of adipocytes in iWAT. Although Rosi induced adipocyte hypertrophy

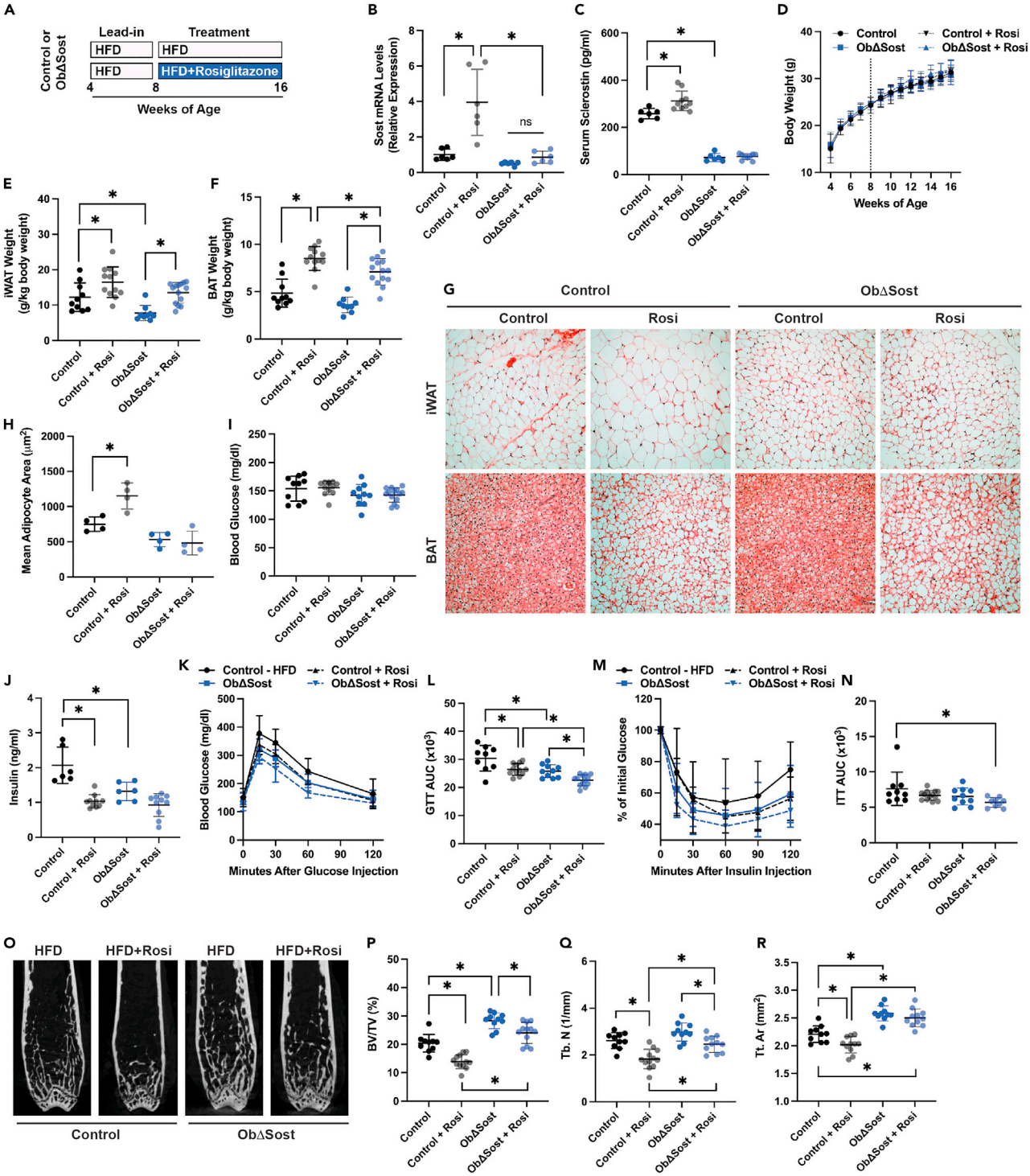

Figure 5. Sost gene deficiency synergizes with the metabolic actions of rosiglitazone

4-week-old male control and ObΔSost mice were fed a high fat diet (HFD, 60% kcal from fat) for 4 weeks and then randomly to continue on an HFD or fed an HFD containing rosiglitazone (100 ppm), which results in treatment with 20 mg/kg/day rosiglitazone.

(A) Schematic of experimental plan.

(B and C) qPCR analysis of Sost mRNA levels in the femur (B, n = 6 mice per group) and serum sclerostin levels (C, n = 6–10 mice per group) at the conclusion of the experiment.

(D) Weekly body weight during the 12-week experiment (n = 10–14 mice per group). The vertical dash lined marks the start of rosiglitazone containing diet.

Figure 5. *Continued*
(E and F) iWAT and BAT tissue weight (n = 10–14 mice per group).
(G) Representative hematoxylin and eosin histological sections of iWAT and BAT (10× original magnification).
(H) Quantification of iWAT adipocyte area (n = 4 mice per group).
(I and J) Quantification of random fed blood glucose levels (I, n = 10–14 mice per group) and serum insulin levels (J, n = 6–10 mice per group).
(K and L) Glucose tolerance testing and area under the curve analysis (n = 9–13 mice per group).
(M and N) Insulin tolerance testing and area under the curve analysis (n = 9–13 mice per group).
(O) Representative microCT images of the distal femur (P-P) MicroCT quantification of trabecular bone volume per tissue volume (BV/TV, P), trabecular number (Tb.N, Q) cortical tissue area (Tt.Ar, R) at the mid-diaphysis (n = 10–11 mice per group). Data presented as mean and standard deviation. *, $p < 0.05$. Data were analyzed by unpaired Student's *t* test or Anova followed by Tukey's multiple comparison post hoc test.

in control mice, adipocyte size was not increased by Rosi in ObΔSost mice (Figures 5G and 5H). This suggests that *Sost* deficiency alters the mechanism of iWAT tissue hypertrophy induced by Rosi. Presumably, Rosi induced a larger increase in preadipocyte proliferation and/or commitment in ObΔSost mice because tissue mass was still increased.

Random fed blood glucose levels were similar across the 4 group (Figure 5I) but consistent with its actions as an insulin sensitizer, serum insulin levels were markedly decreased in control mice treated with Rosi (Figure 5J). Serum insulin levels were also reduced in ObΔSost mice relative to controls but not further reduced by Rosi treatment, but dynamic tests of glucose homeostasis suggested a synergistic interaction between Rosi treatment and *Sost* gene deficiency. Glucose excersions during glucose tolerance testing were reduced in ObΔSost mice and control Rosi treated mice relative controls and were reduced significantly further in ObΔSost mice treated with Rosi (Figures 5K and 5L). Moreover, area under the curve analysis after insulin tolerance testing revealed that insulin sensitivity relative to controls was only significantly improved in ObΔSost mice treated with Rosi (Figures 5L and 5M).

In the distal femur, Rosi resulted in the expected decrease in trabecular bone volume (−31.58 ± 12.60%) in control mice and ObΔSost mice displayed the expected increase in bone volume (+39.01 ± 13.39%, Figures 5O and 5P). Loss of sclerostin function in the context of Rosi treatment offered partial protection in this bone compartment as trabecular bone volume in ObΔSost treated with Rosi was reduced relative to untreated ObΔSost mice (−15.33 ± 13.78%) but was significantly higher than control mice treated with Rosi and trended higher than untreated control mice ($p = 0.052$). More strikingly, although Rosi suppressed cortical bone apposition in control mice, ObΔSost mice were completely resistant to this effect as cortical tissue area was identical in untreated ObΔSost mice and ObΔSost mice treated with Rosi (Figures 5O and 5R). Therefore, suppression of *Sost* expression offers protection against the detrimental effects of Rosi on bone structure and synergizes with the metabolic effects of the drug.

DISCUSSION

In these studies, we pursued mechanisms by which *Sost* gene expression and serum sclerostin levels are controlled. In addition to its well-established local role in the regulation of bone formation,[17,45] our previous work demonstrated that endocrine sclerostin, present in the serum, influences the accumulation of fat mass as well as glucose and lipid metabolism.[18,19] We focused on PPARγ as a result of its fundamental role in metabolic homeostasis,[32] its ability to regulate osteoblast function,[38–40] and the fact that the *Sost* gene promoter contains several PPAR response elements.[38]

Consistent with previous studies that disrupted the expression of *Pparg* in cells of the osteoblast lineage,[38–40] we found that the loss of PPARγ function in mature osteoblasts and osteocytes (Ocn-Cre$^+$ cells) resulted in a high bone mass phenotype. The mutant mice exhibited normal bone structure until age 8 weeks and then developed an increase in trabecular bone volume fraction and cortical tissue cross-sectional area as they approached skeletal maturity. *In vitro* studies and dynamic measures of bone cell function indicated that the high bone mass phenotype was primarily driven by an increase in osteoblast performance as alizarin red staining and the mineral apposition rate were increased. The decrease in osteoclast abundance noted in the mutant mice suggests that a reduction in bone resorption also contributed to the high bone mass phenotype. Of interest, reduced osteoclast numbers were not reported in the other models of PPARγ loss of function in osteoblastic cells,[38,39] though Brun[40] did observe a reduction in carboxyterminal collagen crosslinks indicative of a reduction in osteoclast activity. The delay in the onset of the skeletal phenotype is likely linked to the age-related increase in *Pparg* expression levels in bone tissue.

Alongside the bone phenotype, we also demonstrated that ablating the *Pparg* gene in osteoblasts and osteocytes influences body composition and metabolic homeostasis. At the same time points that bone volume and osteoblastic activity were increased, subcutaneous fat mass was reduced and the morphology of inguinal white adipocytes shifted dramatically toward a beige phenotype marked by increased numbers of multilocular cells and increased UCP1 immuno-reactivity. The lack of a corresponding change in whole body energy expenditure in ΔPparg mice likely relates to the sensitivity of the indirect calorimetry procedure. White adipose contributes only a small fraction to overall resting metabolic rate,[46,47] thus small changes in the metabolic activity of adipocytes over the life of mutant mice may not be measurable by indirect calorimetry. In addition to adipose tissue, muscle and liver in the PPARγ mutants exhibited an increase in insulin sensitivity which likely contributed to the increase in insulin and glucose tolerance in the mutants. Most of these metabolic phenotypes remained evident in PPARγ mutants fed a high fat diet. These results are compatible with two previous descriptions of metabolic changes when PPARγ is targeted in osteoblastic cells. Almeida[48] reported that *Pparg* gene deletion in Prx1^{+} cells (early limb bud mesenchyme and skeletal stem/progenitor cells) resulted in a lack of subcutaneous adipose but the interpretation of these studies is hampered by the concomitant targeting of a subset of white adipose progenitor cells.[49] Similarly, Brun[40] found that *Pparg* gene deletion in DMP1^{+} cells (late osteoblasts and osteocytes) developed a high bone mass and low adipose phenotype with metabolic phenotypes similar to our knockout model.

Mechanistically, Brun[40] proposed that the metabolic phenotypes in 10kb-DMP1-Cre$^{TG/+}$; Pparg$^{loxP/loxP}$ mice resulted from increased production of BMP7 that in turn exerted an endocrine function. In our studies, the levels of SMAD1/5/9 phosphorylation levels, a marker of BMP signaling, were reduced instead of increased in the adipose tissue of mutant mice, suggesting a different mechanism by which PPARγ in osteoblasts and osteocytes affects metabolism. As noted above, the metabolic phenotypes of ΔPparg mice mirror those evident in Sost$^{-/-}$ mice[18] and both *Sost* expression levels in bone and serum sclerostin abundance in the male mutants tracked with the development of the metabolic phenotype. *Sost* mRNA levels and sclerostin serum levels were also reduced in female mutants and male mutants fed a high fat diet whereas the abundance of active β-catenin, indicative of Wnt signaling activation, was increased in the white adipose of ΔPparg mice. Most importantly, raising serum sclerostin levels in ΔPparg mice to a level equivalent to those in control mice, but below those in high fat diet fed mice, via an adeno-associated viral approach was sufficient to normalize the bone, adipose, and metabolic phenotypes of ΔPparg mice. These data indicate that regulation of sclerostin production by PPARγ is the primary mechanism by which the transcription factor in osteoblasts and osteocytes influences metabolism. It should be noted that AAV-mediated Sost overproduction in this study did not increase serum sclerostin levels in control mice (Pparg$^{loxP/loxP}$, 262.8 pg/mL) to the level observed in our previous work using albino C57Bl/6 mice (442.8 pg/mL,[18]). This almost certainly explains the lack of phenotypic differences in bone and metabolic function between Control-AAV-GFP and Control-AAV-Sost. The mechanisms by which PPARγ in bone cells and sclerostin influence adipose tissue browning are actively under-investigation.

The most striking finding in this study was the interaction between *Sost* gene ablation and the actions of rosiglitazone. Several studies have found that activation of PPARγ with thiazolidinediones increases Sost expression *in vitro*,[38,50] which is expected to contribute to the loss of bone mass associated with this therapy as sclerostin neutralizing antibodies ameliorate the deterioration of bone structure in rosiglitazone treated mice.[51,52] We also observed an increase in *Sost* gene expression and serum sclerostin levels following rosiglitazone treatment and found that genetic sclerostin loss of function was sufficient to partially rescue defects in bone structure. The decrease in trabecular bone volume induced by rosiglitazone was cut in half whereas the inhibition of appositional growth in cortical bone by the drug was completely inhibited in ObΔSost mice. The ∼15% decrease in trabecular bone fraction induced by rosiglitazone that persists in ObΔSost indicates other sclerostin-independent mechanisms also contribute to the bone loss.

With regards to the effects on body composition and metabolism, rosiglitazone produced similar relative increases in the mass of the inguinal white adipose and interscapular brown adipose tissue depots in control and ObΔSost mice but the effect on inguinal adipocyte morphology was strikingly different. Although rosiglitazone induced adipocyte hypertrophy in control mice, the adipocytes in ObΔSost mice were smaller and were identical to those in untreated ObΔSost mice. Based on our previous analyses of sclerostin function in adipocytes,[18,53] we suspect that the inhibition of adipocyte hypertrophy in the absence of sclerostin

is secondary to a lower rate of *de novo* fatty acid synthesis. As indicated in the Results, the fact that inguinal mass was still increased in ObΔSost mice suggests that rosiglitazone induced a higher rate of proliferation or progenitor cell commitment in these mice. This is surprising because the loss of sclerostin function inhibits the differentiation of Pdgfrα^{+} adipoprogenitors.[19] It is possible that the increase in inguinal mass was instead driven by another pool of adipoprogenitors that are insensitive to the loss of sclerostin. The comparable changes in the morphology of brown adipocytes in rosiglitazone treated control and ObΔSost mice was not surprising as neither global *Sost* gene ablation or sclerostin overproduction influence the morphology or function of this depot.[18]

The persistence of small adipocytes in the white adipose of ObΔSost mice treated with rosiglitazone may partially explain the synergistic effects evident during glucose tolerance testing and insulin tolerance testing. Small adipocytes are generally considered to be more insulin sensitive than those that have undergone hypertrophy.[54,55] It is also possible that the synergistic effects of rosiglitazone and sclerostin deficiency on glucose homeostasis are derived from effects in the liver. Glucose uptake by skeletal muscle was increased in Sost$^{-/-}$ mice during a hyperinsulinemic-euglycemic clamp[18] and rosiglitazone has been shown to increase insulin sensitivity in skeletal muscle. Additional study would be necessary to discern the contributions of individual tissues to the overall effect on glucose homeostasis observed here. Farrell et al.[51] performed a study similar to ours to examine the interaction between sclerostin and PPARγ activation with rosiglitazone. This study found that sclerostin neutralizing antibodies reduced marrow adipogenesis in response to rosiglitazone and that the antibodies reduced visceral fat mass in both control and rosi-treated animals. However, there was no additive effects nor was there an apparent effect on glucose homeostasis. It should be noted that this study was performed in chow diet-fed (with or without Rosi) SCID Beige mice, that lack a normal immune function. When taken together with our study, this may suggest that the interaction only exists when metabolism homeostasis is compromised as in the high fat diet feeding used here or that immune function is required for the interactions. In future studies, it will be interesting to determine if PPARγ reverse agonists also synergize with sclerostin loss of function and whether Sost gene expression and sclerostin serum abundance correlate with the phosphorylation status of PPARγ.

In summary, these studies elaborate on the mechanism by which sclerostin expression is linked to metabolism as well as the actions of PPARγ in bone and metabolic homeostasis. Further examination of this interaction may have benefits from the treatment of metabolic disease and lead to the development of strategies that mitigate bone loss in the face of anti-diabetic/anti-obesity therapies and perhaps allow for the utilization of lower doses.

Limitations of the study

A potential limitation of this study relates to the use of Cre-mediated recombination in this study. All Cre-expressing lines present caveats related to tissue-specific expression. In this study we did not observe recombination of the Pparg flox allele in tissues outside of bone, but not all tissues were surveyed. A second limitation relates to the use of genetic elimination of *Sost* gene expression in mice treated with rosiglitazone as opposed to pharmacological inhibition with a neutralizing antibody. These studies were meant to show a potential interaction between anti-diabetic therapeutics and sclerostin loss of function. As such a neutralizing antibody approach would have more closely modeled a clinical treatment strategy. Unfortunately, a sclerostin neutralizing antibodies could not be obtained to complete the study.

STAR★METHODS

Detailed methods are provided in the online version of this paper and include the following:

- KEY RESOURCES TABLE
- RESOURCE AVAILABILITY
  - Lead contact
  - Material availability
  - Data and code availability
- EXPERIMENTAL MODEL AND SUBJECT DETAILS
- METHOD DETAILS
  - Cell culture
  - Skeletal analysis
  - Metabolic assays

- Tissue morphometry
- Gene expression studies and western blotting
- QUANTIFICATION AND STATISTICAL ANALYSIS

SUPPLEMENTAL INFORMATION

Supplemental information can be found online at https://doi.org/10.1016/j.isci.2023.106999.

ACKNOWLEDGMENTS

This work was supported by Merit Review Grant BX003724 from the Biomedical Laboratory Research and Development, VA Office of Research and Development to R.C.R.

AUTHOR CONTRIBUTIONS

S.P.K., A.H.S., and R.C.R. designed the experiments. S.P.K., A.H.S., J.G., N.A., N.R.G., S.A., and R.C.R. collected and analyzed data. J.P.S. and M.J.W. provided key experimental materials. S.P.K. and R.C.R analyzed the data and prepared the manuscript.

DECLARATION OF INTERESTS

The authors declare that they have no known competing financial interests or personal relationships that could have appeared to influence the work reported in this article.

INCLUSION AND DIVERSITY

We support inclusive, diverse, and equitable conduct of research.

Received: March 20, 2023
Revised: May 1, 2023
Accepted: May 25, 2023
Published: May 29, 2023

REFERENCES

1. Misra, M., and Klibanski, A. (2014). Endocrine consequences of anorexia nervosa. Lancet Diabetes Endocrinol. *2*, 581–592. https://doi.org/10.1016/S2213-8587(13)70180-3.

2. Hofbauer, L.C., Busse, B., Eastell, R., Ferrari, S., Frost, M., Müller, R., Burden, A.M., Rivadeneira, F., Napoli, N., and Rauner, M. (2022). Bone fragility in diabetes: novel concepts and clinical implications. Lancet Diabetes Endocrinol. *10*, 207–220. https://doi.org/10.1016/S2213-8587(21)00347-8.

3. Kajimura, D., Lee, H.W., Riley, K.J., Arteaga-Solis, E., Ferron, M., Zhou, B., Clarke, C.J., Hannun, Y.A., DePinho, R.A., Guo, X.E., et al. (2013). Adiponectin regulates bone mass via opposite central and peripheral mechanisms through FoxO1. Cell Metab. *17*, 901–915. https://doi.org/10.1016/j.cmet.2013.04.009.

4. Estell, E.G., Le, P.T., Vegting, Y., Kim, H., Wrann, C., Bouxsein, M.L., Nagano, K., Baron, R., Spiegelman, B.M., and Rosen, C.J. (2020). Irisin directly stimulates osteoclastogenesis and bone resorption in vitro and in vivo. Elife *9*, e58172. https://doi.org/10.7554/eLife.58172.

5. Hansen, M.S., and Frost, M. (2022). Alliances of the gut and bone axis. Semin. Cell Dev. Biol. *123*, 74–81. https://doi.org/10.1016/j.semcdb.2021.06.024.

6. Fulzele, K., Riddle, R.C., DiGirolamo, D.J., Cao, X., Wan, C., Chen, D., Faugere, M.C., Aja, S., Hussain, M.A., Brüning, J.C., and Clemens, T.L. (2010). Insulin receptor signaling in osteoblasts regulates postnatal bone acquisition and body composition. Cell *142*, 309–319. https://doi.org/10.1016/j.cell.2010.06.002.

7. Dirckx, N., Moorer, M.C., Clemens, T.L., and Riddle, R.C. (2019). The role of osteoblasts in energy homeostasis. Nat. Rev. Endocrinol. *15*, 651–665. https://doi.org/10.1038/s41574-019-0246-y.

8. Lee, N.K., Sowa, H., Hinoi, E., Ferron, M., Ahn, J.D., Confavreux, C., Dacquin, R., Mee, P.J., McKee, M.D., Jung, D.Y., et al. (2007). Endocrine regulation of energy metabolism by the skeleton. Cell *130*, 456–469. https://doi.org/10.1016/j.cell.2007.05.047.

9. Ferron, M., McKee, M.D., Levine, R.L., Ducy, P., and Karsenty, G. (2012). Intermittent injections of osteocalcin improve glucose metabolism and prevent type 2 diabetes in mice. Bone *50*, 568–575. https://doi.org/10.1016/j.bone.2011.04.017.

10. Mera, P., Laue, K., Ferron, M., Confavreux, C., Wei, J., Galan-Diez, M., Lacampagne, A., Mitchell, S.J., Mattison, J.A., Chen, Y., et al. (2016). Osteocalcin signaling in myofibers is necessary and sufficient for optimum adaptation to exercise. Cell Metab. *23*, 1078–1092. https://doi.org/10.1016/j.cmet.2016.05.004.

11. Mera, P., Laue, K., Wei, J., Berger, J.M., and Karsenty, G. (2016). Osteocalcin is necessary and sufficient to maintain muscle mass in older mice. Mol. Metab. *5*, 1042–1047. https://doi.org/10.1016/j.molmet.2016.07.002.

12. Balemans, W., Ebeling, M., Patel, N., Van Hul, E., Olson, P., Dioszegi, M., Lacza, C., Wuyts, W., Van Den Ende, J., Willems, P., et al. (2001). Increased bone density in sclerosteosis is due to the deficiency of a novel secreted protein (SOST). Hum. Mol. Genet. *10*, 537–543.

13. Balemans, W., Patel, N., Ebeling, M., Van Hul, E., Wuyts, W., Lacza, C., Dioszegi, M., Dikkers, F.G., Hildering, P., Willems, P.J., et al. (2002). Identification of a 52 kb deletion downstream of the SOST gene in patients with van Buchem disease. J. Med. Genet. *39*, 91–97. https://doi.org/10.1136/jmg.39.2.91.

14. Staehling-Hampton, K., Proll, S., Paeper, B.W., Zhao, L., Charmley, P., Brown, A., Gardner, J.C., Galas, D., Schatzman, R.C., Beighton, P., et al. (2002). A 52-kb deletion in the SOST-MEOX1 intergenic region on 17q12-q21 is associated with van Buchem disease in the Dutch population. Am. J. Med. Genet. *110*, 144–152. https://doi.org/10.1002/ajmg.10401.

15. Ellies, D.L., Viviano, B., McCarthy, J., Rey, J.P., Itasaki, N., Saunders, S., and Krumlauf, R. (2006). Bone density ligand, Sclerostin, directly interacts with LRP5 but not LRP5G171V to modulate Wnt activity. J. Bone Miner. Res. *21*, 1738–1749. https://doi.org/10.1359/jbmr.060810.

16. Semënov, M., Tamai, K., and He, X. (2005). SOST is a ligand for LRP5/LRP6 and a Wnt signaling inhibitor. J. Biol. Chem. *280*, 26770–26775. https://doi.org/10.1074/jbc.M504308200.

17. Li, X., Ominsky, M.S., Niu, Q.T., Sun, N., Daugherty, B., D'Agostin, D., Kurahara, C., Gao, Y., Cao, J., Gong, J., et al. (2008). Targeted deletion of the sclerostin gene in mice results in increased bone formation and bone strength. J. Bone Miner. Res. *23*, 860–869. https://doi.org/10.1359/jbmr.080216.

18. Kim, S.P., Frey, J.L., Li, Z., Kushwaha, P., Zoch, M.L., Tomlinson, R.E., Da, H., Aja, S., Noh, H.L., Kim, J.K., et al. (2017). Sclerostin influences body composition by regulating catabolic and anabolic metabolism in adipocytes. Proc. Natl. Acad. Sci. USA *114*, E11238–E11247. https://doi.org/10.1073/pnas.1707876115.

19. Kim, S.P., Da, H., Wang, L., Taketo, M.M., Wan, M., and Riddle, R.C. (2021). Bone-derived sclerostin and Wnt/beta-catenin signaling regulate PDGFRalpha(+) adipoprogenitor cell differentiation. FASEB J *35*, e21957. https://doi.org/10.1096/fj.202100691R.

20. Amrein, K., Amrein, S., Drexler, C., Dimai, H.P., Dobnig, H., Pfeifer, K., Tomaschitz, A., Pieber, T.R., and Fahrleitner-Pammer, A. (2012). Sclerostin and its association with physical activity, age, gender, body composition, and bone mineral content in healthy adults. J. Clin. Endocrinol. Metab. *97*, 148–154. https://doi.org/10.1210/jc.2011-2152.

21. Urano, T., Shiraki, M., Ouchi, Y., and Inoue, S. (2012). Association of circulating sclerostin levels with fat mass and metabolic disease–related markers in Japanese postmenopausal women. J. Clin. Endocrinol. Metab. *97*, E1473–E1477. https://doi.org/10.1210/jc.2012-1218.

22. Daniele, G., Winnier, D., Mari, A., Bruder, J., Fourcaudot, M., Pengou, Z., Tripathy, D., Jenkinson, C., and Folli, F. (2015). Sclerostin and insulin resistance in prediabetes: evidence of a cross talk between bone and glucose metabolism. Diabetes Care *38*, 1509–1517. https://doi.org/10.2337/dc14-2989.

23. Rianon, N.J., Smith, S.M., Lee, M., Pervin, H., Musgrave, P., Watt, G.P., Nader, S., Khosla, S., Ambrose, C.G., McCormick, J.B., and Fisher-Hoch, S.P. (2018). Glycemic control and bone turnover in older Mexican Americans with type 2 diabetes. J. Osteoporos. *2018*, 7153021. https://doi.org/10.1155/2018/7153021.

24. Yu, O.H.Y., Richards, B., Berger, C., Josse, R.G., Leslie, W.D., Goltzman, D., Kaiser, S.M., Kovacs, C.S., and Davison, K.S. (2017). The association between sclerostin and incident type 2 diabetes risk: a cohort study. Clin. Endocrinol. *86*, 520–525. https://doi.org/10.1111/cen.13300.

25. Cosman, F., Crittenden, D.B., Adachi, J.D., Binkley, N., Czerwinski, E., Ferrari, S., Hofbauer, L.C., Lau, E., Lewiecki, E.M., Miyauchi, A., et al. (2016). Romosozumab treatment in postmenopausal women with osteoporosis. N. Engl. J. Med. *375*, 1532–1543. https://doi.org/10.1056/NEJMoa1607948.

26. McClung, M.R., Grauer, A., Boonen, S., Bolognese, M.A., Brown, J.P., Diez-Perez, A., Langdahl, B.L., Reginster, J.Y., Zanchetta, J.R., Wasserman, S.M., et al. (2014). Romosozumab in postmenopausal women with low bone mineral density. N. Engl. J. Med. *370*, 412–420. https://doi.org/10.1056/NEJMoa1305224.

27. Fairfield, H., Falank, C., Harris, E., Demambro, V., McDonald, M., Pettitt, J.A., Mohanty, S.T., Croucher, P., Kramer, I., Kneissel, M., et al. (2018). The skeletal cell-derived molecule sclerostin drives bone marrow adipogenesis. J. Cell. Physiol. *233*, 1156–1167. https://doi.org/10.1002/jcp.25976.

28. Baek, K., Hwang, H.R., Park, H.J., Kwon, A., Qadir, A.S., Ko, S.H., Woo, K.M., Ryoo, H.M., Kim, G.S., and Baek, J.H. (2014). TNF-alpha upregulates sclerostin expression in obese mice fed a high-fat diet. J. Cell. Physiol. *229*, 640–650. https://doi.org/10.1002/jcp.24487.

29. Pacicca, D.M., Brown, T., Watkins, D., Kover, K., Yan, Y., Prideaux, M., and Bonewald, L. (2019). Elevated glucose acts directly on osteocytes to increase sclerostin expression in diabetes. Sci. Rep. *9*, 17353. https://doi.org/10.1038/s41598-019-52224-3.

30. Fang, L., Zhang, M., Li, Y., Liu, Y., Cui, Q., and Wang, N. (2016). PPARgene: a database of experimentally verified and computationally predicted PPAR target genes. PPAR Res. *2016*, 6042162. https://doi.org/10.1155/2016/6042162.

31. Tontonoz, P., Graves, R.A., Budavari, A.I., Erdjument-Bromage, H., Lui, M., Hu, E., Tempst, P., and Spiegelman, B.M. (1994). Adipocyte-specific transcription factor ARF6 is a heterodimeric complex of two nuclear hormone receptors, PPAR gamma and RXR alpha. Nucleic Acids Res. *22*, 5628–5634. https://doi.org/10.1093/nar/22.25.5628.

32. Ahmadian, M., Suh, J.M., Hah, N., Liddle, C., Atkins, A.R., Downes, M., and Evans, R.M. (2013). PPARgamma signaling and metabolism: the good, the bad and the future. Nat. Med. *19*, 557–566. https://doi.org/10.1038/nm.3159.

33. Tontonoz, P., Hu, E., and Spiegelman, B.M. (1994). Stimulation of adipogenesis in fibroblasts by PPAR gamma 2, a lipid-activated transcription factor. Cell *79*, 1147–1156. https://doi.org/10.1016/0092-8674(94)90006-x.

34. Wang, F., Mullican, S.E., DiSpirito, J.R., Peed, L.C., and Lazar, M.A. (2013). Lipoatrophy and severe metabolic disturbance in mice with fat-specific deletion of PPARgamma. Proc. Natl. Acad. Sci. USA *110*, 18656–18661. https://doi.org/10.1073/pnas.1314863110.

35. Lecka-Czernik, B., Gubrij, I., Moerman, E.J., Kajkenova, O., Lipschitz, D.A., Manolagas, S.C., and Jilka, R.L. (1999). Inhibition of Osf2/Cbfa1 expression and terminal osteoblast differentiation by PPARgamma2. J. Cell. Biochem. *74*, 357–371.

36. Shockley, K.R., Lazarenko, O.P., Czernik, P.J., Rosen, C.J., Churchill, G.A., and Lecka-Czernik, B. (2009). PPARgamma2 nuclear receptor controls multiple regulatory pathways of osteoblast differentiation from marrow mesenchymal stem cells. J. Cell. Biochem. *106*, 232–246. https://doi.org/10.1002/jcb.21994.

37. Bilezikian, J.P., Josse, R.G., Eastell, R., Lewiecki, E.M., Miller, C.G., Wooddell, M., Northcutt, A.R., Kravitz, B.G., Paul, G., Cobitz, A.R., et al. (2013). Rosiglitazone decreases bone mineral density and increases bone turnover in postmenopausal women with type 2 diabetes mellitus. J. Clin. Endocrinol. Metab. *98*, 1519–1528. https://doi.org/10.1210/jc.2012-4018.

38. Baroi, S., Czernik, P.J., Chougule, A., Griffin, P.R., and Lecka-Czernik, B. (2021). PPARG in osteocytes controls sclerostin expression, bone mass, marrow adiposity and mediates TZD-induced bone loss. Bone *147*, 115913. https://doi.org/10.1016/j.bone.2021.115913.

39. Cao, J., Ding, K., Pan, G., Rosario, R., Su, Y., Bao, Y., Zhou, H., Xu, J., McGee Lawrence, M.E., Hamrick, M.W., et al. (2020). Deletion of PPARgamma in mesenchymal lineage cells protects against aging-induced cortical bone loss in mice. J. Gerontol. A Biol. Sci. Med. Sci. *75*, 826–834. https://doi.org/10.1093/gerona/glaa049.

40. Brun, J., Berthou, F., Trajkovski, M., Maechler, P., Foti, M., and Bonnet, N. (2017). Bone regulates browning and energy metabolism through mature osteoblast/osteocyte PPARgamma expression. Diabetes *66*, 2541–2554. https://doi.org/10.2337/db17-0116.

41. Jho, E.H., Zhang, T., Domon, C., Joo, C.K., Freund, J.N., and Costantini, F. (2002). Wnt/beta-catenin/Tcf signaling induces the transcription of Axin2, a negative regulator of the signaling pathway. Mol. Cell Biol. *22*, 1172–1183.

42. Brunkow, M.E., Gardner, J.C., Van Ness, J., Paeper, B.W., Kovacevich, B.R., Proll, S., Skonier, J.E., Zhao, L., Sabo, P.J., Fu, Y., et al. (2001). Bone dysplasia sclerosteosis results from loss of the SOST gene product, a novel cystine knot-containing protein. Am. J. Hum. Genet. *68*, 577–589.

43. Nissen, S.E., and Wolski, K. (2007). Effect of rosiglitazone on the risk of myocardial infarction and death from cardiovascular causes. N. Engl. J. Med. *356*, 2457–2471. https://doi.org/10.1056/NEJMoa072761.

44. Economides, A.N., Frendewey, D., Yang, P., Dominguez, M.G., Dore, A.T., Lobov, I.B., Persaud, T., Rojas, J., McClain, J., Lengyel, P., et al. (2013). Conditionals by inversion provide a universal method for the generation of conditional alleles. Proc. Natl.

Acad. Sci. USA *110*, E3179–E3188. https://doi.org/10.1073/pnas.1217812110.

45. Yee, C.S., Manilay, J.O., Chang, J.C., Hum, N.R., Murugesh, D.K., Bajwa, J., Mendez, M.E., Economides, A.E., Horan, D.J., Robling, A.G., and Loots, G.G. (2018). Conditional deletion of Sost in MSC-derived lineages identifies specific cell-type contributions to bone mass and B-cell development. J. Bone Miner. Res. *33*, 1748–1759. https://doi.org/10.1002/jbmr.3467.

46. Elia, M. (1992). Organ and tissue contribution to metabolic rate. In Energy metabolism: tissue determinants and cellular corollaries, J.M. Kinney and H.N. Tucker, eds. (Raven Press), pp. 61–80.

47. Wang, Z., Ying, Z., Bosy-Westphal, A., Zhang, J., Schautz, B., Later, W., Heymsfield, S.B., and Müller, M.J. (2010). Specific metabolic rates of major organs and tissues across adulthood: evaluation by mechanistic model of resting energy expenditure. Am. J. Clin. Nutr. *92*, 1369–1377. https://doi.org/10.3945/ajcn.2010.29885.

48. Almeida, M., Kim, H.N., Han, L., Zhou, D., Thostenson, J., Porter, R.M., Ambrogini, E., Manolagas, S.C., and Jilka, R.L. (2020). Increased marrow adipogenesis does not contribute to age-dependent appendicular bone loss in female mice. Aging Cell *19*, e13247. https://doi.org/10.1111/acel.13247.

49. Sanchez-Gurmaches, J., Hsiao, W.Y., and Guertin, D.A. (2015). Highly selective in vivo labeling of subcutaneous white adipocyte precursors with Prx1-Cre. Stem Cell Rep. *4*, 541–550. https://doi.org/10.1016/j.stemcr.2015.02.008.

50. Mieczkowska, A., Baslé, M.F., Chappard, D., and Mabilleau, G. (2012). Thiazolidinediones induce osteocyte apoptosis by a G protein-coupled receptor 40-dependent mechanism. J. Biol. Chem. *287*, 23517–23526. https://doi.org/10.1074/jbc.M111.324814.

51. Farrell, M., Fairfield, H., Costa, S., D'Amico, A., Falank, C., Brooks, D.J., and Reagan, M.R. (2021). Sclerostin-neutralizing antibody treatment rescues negative effects of rosiglitazone on mouse bone parameters. J. Bone Miner. Res. *36*, 158–169. https://doi.org/10.1002/jbmr.4170.

52. Lee, J.Y., Yang, J.Y., and Kim, S.W. (2021). Bone lining cells could Be sources of bone marrow adipocytes. Front. Endocrinol. *12*, 766254. https://doi.org/10.3389/fendo.2021.766254.

53. Kim, S.P., Da, H., Li, Z., Kushwaha, P., Beil, C., Mei, L., Xiong, W.C., Wolfgang, M.J., Clemens, T.L., and Riddle, R.C. (2019). Lrp4 expression by adipocytes and osteoblasts differentially impacts sclerostin's endocrine effects on body composition and glucose metabolism. J. Biol. Chem. *294*, 6899–6911. https://doi.org/10.1074/jbc.RA118.006769.

54. Salans, L.B., Knittle, J.L., and Hirsch, J. (1968). The role of adipose cell size and adipose tissue insulin sensitivity in the carbohydrate intolerance of human obesity. J. Clin. Invest. *47*, 153–165. https://doi.org/10.1172/JCI105705.

55. Kim, J.I., Huh, J.Y., Sohn, J.H., Choe, S.S., Lee, Y.S., Lim, C.Y., Jo, A., Park, S.B., Han, W., and Kim, J.B. (2015). Lipid-overloaded enlarged adipocytes provoke insulin resistance independent of inflammation. Mol. Cell Biol. *35*, 1686–1699. https://doi.org/10.1128/MCB.01321-14.

56. He, W., Barak, Y., Hevener, A., Olson, P., Liao, D., Le, J., Nelson, M., Ong, E., Olefsky, J.M., and Evans, R.M. (2003). Adipose-specific peroxisome proliferator-activated receptor gamma knockout causes insulin resistance in fat and liver but not in muscle. Proc. Natl. Acad. Sci. USA *100*, 15712–15717. https://doi.org/10.1073/pnas.2536828100.

57. Zhang, M., Xuan, S., Bouxsein, M.L., von Stechow, D., Akeno, N., Faugere, M.C., Malluche, H., Zhao, G., Rosen, C.J., Efstratiadis, A., and Clemens, T.L. (2002). Osteoblast-specific knockout of the insulin-like growth factor (IGF) receptor gene reveals an essential role of IGF signaling in bone matrix mineralization. J. Biol. Chem. *277*, 44005–44012. https://doi.org/10.1074/jbc.M208265200 M208265200.

58. Sands, M.S. (2011). AAV-mediated liver-directed gene therapy. Methods Mol. Biol. *807*, 141–157. https://doi.org/10.1007/978-1-61779-370-7_6.

59. Bouxsein, M.L., Boyd, S.K., Christiansen, B.A., Guldberg, R.E., Jepsen, K.J., and Müller, R. (2010). Guidelines for assessment of bone microstructure in rodents using micro-computed tomography. J. Bone Miner. Res. *25*, 1468–1486. https://doi.org/10.1002/jbmr.141.

60. Dempster, D.W., Compston, J.E., Drezner, M.K., Glorieux, F.H., Kanis, J.A., Malluche, H., Meunier, P.J., Ott, S.M., Recker, R.R., and Parfitt, A.M. (2013). Standardized nomenclature, symbols, and units for bone histomorphometry: a 2012 update of the report of the ASBMR Histomorphometry Nomenclature Committee. J. Bone Miner. Res. *28*, 2–17. https://doi.org/10.1002/jbmr.1805.

61. Lusk, G. (1928). The Elements of the Science of Nutrition (WB Saunders).

STAR★METHODS

KEY RESOURCES TABLE

REAGENT or RESOURCE	SOURCE	IDENTIFIER
Antibodies		
Mouse anti-Actin	Cell Signaling Tech	3700; RRID:AB_2242334
Rabbit anti-Acetyl-CoA Carboxylase	Cell Signaling Tech	3676; RRID:AB_2219397
Rabbit anti-Fatty acid Synthase	Cell Signaling Tech	3180; RRID:AB_2100796
Total OXPHOS Rodent WB Antibody Cocktail	Abcam	Ab110411; RRID:AB_2756818
Rabbit anti-Phospho-Akt – Ser473	Cell Signaling Tech	4060: RRID:AB_2315049
Rabbit anti-Akt	Cell Signaling Tech	4685; RRID:AB_2225340
Rabbit anti-Non-phospho (Active) β-Catenin	Cell Signaling Tech	8814; RRID:AB_11127203
Rabbit anti-B-catenin	Cell Signaling Tech	8480; RRID:AB_11127855
Rabbit anti-Phospho-Smad1/5/9	Cell Signaling Tech	13820; RRID:AB_2493181
Rabbit anti-Smad1	Cell Signaling Tech	6944; RRID:AB_10858882
Rabbit anti-Ucp1	Abcam	ab10983; RRID:AB_2241462
Bacterial and virus strains		
AAV8-m-SOST	Vector Biolabs	AAV-272868
AAV8-Cag-GFP	Vector Biolabs	7075
Ad-CMV-CRE	Vector Biolabs	1045
Ad-GFP	Vector Biolabs	1060
Chemicals, peptides, and recombinant proteins		
Type I Collagenase	Worthington Biochemical Corp	4197
Calcein	Sigma	C0875
Alizarin Red S	Sigma	A3882
TRizol	ThermoFisher	15596026
Human Insulin	Sigma Aldrich	I0908
Rosiglitazone	Cayman Chemical	71740
a-Minimal Essential Medium	Corning	15-012-CV
Fetal Bovine Serum	Corning	35-010-CV
Penicillin/streptomycin antibiotic	ThermoFisher	15140148
Critical commercial assays		
iScript cDNA Synthesis kit	BioRad	1708890
iQ Sybr Green Supermix for qPCR	BioRad	1708880
Serum Triglyceride Determination Kit	Sigma Aldrich	TR0100
Free Fatty Acid Quantitation Kit	Sigma Aldrich	MAK044
Cholesterol Quantitation Kit	Sigma Aldrich	MAK043

(*Continued on next page*)

Continued

REAGENT or RESOURCE	SOURCE	IDENTIFIER
Mouse Insulin Elisa	ALPCO	80-INSMS-E01
Mouse/Rat Sost Quantikine Elisa	R&D Systems	MSST00
Experimental models: Cell lines		
Ocy454 osteocyte-like cells	Dr. Divieti-Pajevic, Boston University	N/A
Primary calvarial osteoblasts	This Paper	N/A
Experimental models: Organisms/strains		
Pparg flox mice; B6.129-Ppargtm2Rev/J	Jackson Lab	IMSR_JAX:004584; RRID:IMSR_JAX:004584
Osteocalcin-Cre+ Mice	Laboratory Stocks	RRID:MGI:6198741
Sost iCoin mice	Aris Economides; Regeneron	N/A
Oligonucleotides		
See table for oligonucleotide sequences		
Software and algorithms		
Prism 9	Graphpad	N/A
ImageJ	https://imagej.nih.gov	N/A
NRecon	Bruker	N/A
CTan	Bruker	N/A
Bioquant Osteo 21.5	BioQuant	N/A

RESOURCE AVAILABILITY

Lead contact

Further information and requests for reagents and resources should be directed to and will be fulfilled by the lead contact, Ryan Riddle (rriddle@som.umaryland.edu).

Material availability

All materials in this study will be made available on request to the lead contact.

Data and code availability

All data reported in this paper will be shared by the lead contact upon request.

This paper does not report original code.

EXPERIMENTAL MODEL AND SUBJECT DETAILS

Mouse models - The Institutional Animal Care and Use Committee of The Johns Hopkins University and the The University of Maryland School of Medicine approved all procedures involving mice. Pparg$^{flox/flox}$ mice[56] were obtained from The Jackson Laboratory (Strain #004584, Pparg^{tm2Rev}/J). Sost^{iCOIN} mice[44,45] were provided by Dr. Aris Economides. To generate osteoblast/osteocyte-specific mutants, mice were crossed with Osteocalcin-Cre mice.[57] PCR analysis of tail biopsy specimens was used to confirm genotypes. All mice were maintained on a C57Bl/6 background. Mice were house on ventilated racks on a 14 h light/10 h dark cycle and fed *ad libitum* with a standard chow diet (Extruded Global Rodent Diet, Harlan Laboratories). For the diet-induced obesity studies, male mice were fed a 60% high-fat diet (D12492, Research Diets) from 4 weeks of age to 16 weeks of age. For rosiglitazone studies, rosiglitazone (100 ppm) was added to the 60% high fat diet, which results in treatment with 20 mg/kg/day rosiglitazone. Mice were fed the high fat diet from 4 weeks of age to 8 weeks of age before feeding the rosiglitazone diet for an additional 8 weeks. To raise circulating sclerostin levels, male control and Pparg mutant mice were injected with adeno-associated viral constructs (AAV8) directing the expression of a Sost transgene or green fluorescent protein (Vector Biolabs) from the liver.[58] Mice were injected with 10^9 plaque-forming units of AAV8 constructs in phosphate-buffered saline via the tail vein as previously described.[18]

METHOD DETAILS

Cell culture

Calvarial osteoblasts were isolated from 1-3 day old mixed sex mouse neonates sexes by serial digestion in 1.8 mg/mL collagenase type I (Worthington Biochemical) and cultured in α-minimal essential medium containing 10% serum. For gene deletion, cell cultures were infected with adenovirus encoding Cre recombinase or green fluorescent protein as a control at a multiplicity of infection of 100. To induce osteoblastic differentiation, culture medium was supplemented with 10 mM β-glycerol phosphate and 50 μg/mL ascorbic acid. Osteocyte-like Ocy454 cells (provided by Dr. Divieti-Pajevic, Boston University) were cultured on type I rat tail collagen (BD Biosciences) coated dishes in α-MEM supplemented with 10% FBS at 33°C. For experiments, Ocy454 cells were seeded at 125,000 cells/cm^2 into a tissue culture treated vessel and maintained at 37°C and 5% CO_2 for a minimum of 24 h before treating with PPARγ agonists.

Skeletal analysis

Bone architecture was assessed via high resolution micro-tomographic analysis (Skyscan 1275, Bruker) of the femur of both male and female mice. Scanning was performed in accordance with the recommendations of the American Society for Bone and Mineral Research (ASBMR).[59] Femurs were scanned with an isotropic voxel size of 10 μm at 65 keV and 153 μA using a 1.0 mm aluminum filter. Trabecular bone structure was assessed in the distal femur in a 2 mm region of interest 500 μm proximal to the growth plate. Cortical bone structure was assessed in a 500 μm region of interest centered at the femoral mid-diaphysis.

For dynamic histomorphometric analyses of bone formation parameters, mice received IP injections (100 μL) of calcein (10 mg/kg) and alizarin red (30 mg/kg) 10 and 3 days before sacrifice, respectively. Hindlimbs were collected, cleaned of soft tissue, and fixed in ethanol before embedding in methyl-methacrylate and sectioning. TRAP staining and quantification of marrow adipocytes were performed on sections of femurs that were decalcified in 14% Ethylenediaminetetraacetic acid for 14 days. All skeletal histological analyses were performed at standardized sites under the growth plate with BIOQUANT OSTEO 21.5 software (BIOQUANT) in accordance with the recommendations of the ASBMR.[60]

Metabolic assays

Lean tissue and fat pad were collected at necropsy, weighted, and fixed in 4% paraformaldehyde for histological examination or used for RNA or protein extraction. Indirect calorimetry was conducted in a Comprehensive Lab Animal Monitoring System (Columbus Instruments). Calorimetry, daily body weight, and daily food intake data were acquired during a 4-day experimental period. Data from the first 3 days was used to confirm acclimation to the calorimetry chamber, and the fourth day was used for analyses. Rates of oxygen consumption (VO_2, mL/kg/h) and carbon dioxide production (VCO_2) were measured for each chamber every 20 min throughout the study. Respiratory exchange ratio (RER = VCO_2 / VO_2) was calculated by Oxymax software (v. 4.90) to estimate relative oxidation of carbohydrate (RER = 1.0) versus fat (RER approaching 0.7), not accounting for protein oxidation. Energy expenditure was calculated as EE = VO_2 x [3.815 + (1.232 x RER)][61] and normalized for subject lean body mass (kcal/kg/hr). Serum tryiglycerides, free fatty acids, and cholesterol were measured by colorimetric assays (Sigma). Serum sclerostin (R&D Systems) and insulin (Alpco) were measured by ELISA. Blood glucose levels were measured using a Contour hand-held glucometer (Ascensia). All baseline blood glucose or serum measurements were collected 3 h after the initiation of the light cycle. For glucose tolerance testing, glucose (2 g/kg body weight or 1 g/kg for high fat diet mice) was injected IP after a 6 h fast. For insulin tolerance testing, 0.4 U/kg body weight or 1 U/kg for high fat diet mice) was injected IP after a 4 h fast.

Tissue morphometry

Tissues, including white and brown fat pads, liver, and pancreas, were fixed overnight in 4% paraformaldehyde overnight at 4°C before washing with phosphate buffered saline and further fixation in 70% ethanol. Tissues were embedded in paraffin, sectioned, and stained with hematoxylin and eosin according to standard techniques. Adipocyte size and pancreatic islet area were quantified using ImageJ. Immunohistochemical detection of UCP1 (Abcam ab10983, 1:500) was performed using 3,3'-diaminobenzidine (DAB, Vector laboratories).

Gene expression studies and western blotting

For RNA isolation, femur, adipose, and liver were added to TRIzol (Invitrogen) and then snap-frozen in liquid nitrogen and stored at -80°C. For the femur, the proximal end of the femur was removed with scissors and the marrow was flushed with PBS before adding TRIzol. Cell cultures were washed with phosphate-buffered saline and then scaped into TRIzol. Tissues were homogenized in TRIzol prior to purification. Samples collected from adipose tissue were centrifuged for 10 min at 12,000xg to remove excess lipid. Reverse transcriptase reactions were carried out using 1 μg of RNA and the iScript cDNA Synthesis system (Bio-Rad). Real-time qPCR was carried out using iQ Sybr Green Supermix (Bio-Rad) using primer sequences obtained from PrimerBank (http://pga.mgh.harvard.edu/primerbank/index.html). Sequences are available in table. Reactions were normalized to endogenous 18S reference transcripts. For western blotting, tissue samples were snap frozen in liquid nitrogen, homogenized in cell lysis buffer, and prepared for western blotting according to standard techniques. Details on antibodies can be found in the supplemental information.

qPCR Primers

Gene	Forward Primer	Reverse Primer
18S	CTTAGAGGGACAAGTGGCG	ACGCTGAGCCAGTCAGTGTA
Acaca	CTCCCGATTCATAATTGGGTCTG	TCGACCTTGTTTTACTAGGTGC
Atp5a1	TCTCCATGCCTCTAACACTCG	CCAGGTCAACAGACGTGTCAG
Acadl	TTTCCTCGGAGCATGACATTTT	GCCAGCTTTTTCCCAGACCT
Axin2	TGACTCTCCTTCCAGATCCCA	TGCCCACACTAGGCTGACA
Bmp2	GGGACCCGCTGTCTTCTAGT	TCAACTCAAATTCGCTGAGGAC
Bmp4	ATTCCTGGTAACCGAATGCTG	CCGGTCTCAGGTATCAAACTAGC
Bmp7	CCTGTCCATCTTAGGGTTGCC	GGCCTTGTAGGGGTAGGAGA
Bmpr1	TGGCACTGGTATGAAATCAGAC	CAAGGTATCCTCTGGTGCTAAAG
Ccl2	TAAAAACCTGGATCGGAACCAAA	GCATTAGCTTCAGATTTACGGGT
Ccl3	TGTACCATGACACTCTGCAAC	CAACGATGAATTGGCGTGGAA
Ccl4	TTCCTGCTGTTTCTCTTACACCT	CTGTCTGCCTCTTTTGGTCAG
Cd36	ATGGGCTGTGATCGGAACTG	TTTGCCACGTCATCTGGGTTT
Cpt1a	TGGCATCATCACTGGTGTGTT	GTCTAGGGTCCGATTGATCTTTG
Ctnnb1	ATGGAGCCGGACAGAAAAGC	TGGGAGGTGTCAACATCTTCTT
Fabp4	AAGGTGAAGAGCATCATAACCCT	TCACGCCTTTCATAACACATTCC
Fasn	GGAGGTGGTGATAGCCGGTAT	TGGGTAATCCATAGAGCCCAG
Il1b	GAAATGCCACCTTTTGACAGTG	TGGATGCTCTCATCAGGACAG
Il6	CTGCAAGAGACTTCCATCCAG	AGTGGTATAGACAGGTCTGTTGG
Il10	CTTACTGACTGGCATGAGGATCA	GCAGCTCTAGGAGCATGTGG
Mlxipl	AGATGGAGAACCGACGTATCA	ACTGAGCGTGCTGACAAGTC
Ppara	AACATCGAGTGTCGAATATGTGG	CCGAATAGTTCGCCGAAAGAA
Pparg	GGAAGACCACTCGCATTCCTT	GTAATCAGCAACCATTGGGTCA
Ppargc1a	TATGGAGTGACATAGAGTGTGCT	CCACTTCAATCCACCCAGAAAG
Prdm16	CCACCAGCGAGGACTTCAC	GGAGGACTCTCGTAGCTCGAA
Opg	GTGAAGCAGGAGTGCAAC	GCAAACTGTGTTTCGCTC
Osterix	ATGGCGTCCTCTCTGCTTG	TGAAAGGTCAGCGTATGGCTT
Osteocalcin	GAAAA GCCTTCATGTCCAAG	AAAGCCGAGCTGCCAGAGTTT
RankL	TGTACTTTCGAGCGCAGATG	ACATCCAACCATGAGCCTTC
Runx2	CCAAATTTGCCTAACAGAATG	GAGGCTGTGGTTTCAAAGCA
Scd1	TTCTTGCGATACACTCTGGTGC	CGGGATTGAATGTTCTTGTCGT
Sost	AGCCTTCAGGAATGATGCCAC	CTTTGGCGTCATAGGGATGGT
Srebf1	TGACCCGGCTATTCCGTGA	CTGGGCTGAGCAATACAGTTC
Tnf	CAGGCGGTGCCTATGTCTC	CGATCACCCCGAAGTTCAGTAG
Ucp1	GTGAACCCGACAACTTCCGAA	TGCCAGGCAAGCTGAAACTC

QUANTIFICATION AND STATISTICAL ANALYSIS

Data were collected in a blinded fashion for all animal studies. Data are represented as mean ± standard deviation. Data were graphed and analyzed using Prism Graphpad 9.0. Statistical analyses were performed using unpaired, two-tailed Student's t or ANOVA followed by Tukey's multiple comparison post hoc tests. A p value less that 0.05 was considered significant. In all figures, * $p \leq 0.05$.